

The influence of morphology, AGN and environment on the quenching histories of galaxies



Rebecca Jane Smethurst
Pembroke College
University of Oxford

A thesis submitted for the degree of
Doctor of Philosophy
Michaelmas 2016

Oy with the poodles already!

Acknowledgements

Thank ALLL TEH people. Including, for inspiration and the help with perseverance: T. Swift, B. Springsteen, C. Martin et al., Dr M. Grey, L. Gilmore, R. Gilmore, A. Haim et al., E. Sheeran,

Abstract

GZ shit happens.

Contents

1	Introduction	1
1.1	Galaxy Zoo	3
1.1.1	Defining the GZ2-GALEX main galaxy sample	6
2	STARPY: Bayesian inference of a galaxy’s star formation history	7
2.1	Star Formation History Models	7
2.2	Probabilistic Fitting Methods	12
2.3	Testing STARPY	13
2.4	Speeding up STARPY	16
2.5	POPSTARPY: studying populations of galaxies with STARPY	18
2.5.1	Alternative Hierarchical Bayesian approach	20
3	The morphological dependance of quenching	26
3.1	The Red Sample	28
3.2	Green Valley Galaxies	31
3.3	Blue Cloud Galaxies	34
3.3.1	Discussion	37
4	Black hole-galaxy co-evolution in the context of quenching	38
4.1	Rapid, recent quenching within a population of Type 2 AGN host galaxies	38
4.1.1	AGN Sample	38
4.1.2	Results	43
4.1.3	Discussion	46
4.2	Bulgeless galaxies hosting growing black holes	50
4.2.1	Observational Data	50
4.2.1.1	AGN Selection	50
4.2.1.2	Selecting disk-dominated AGN host galaxies	51
4.2.1.3	Spectra	52
4.2.2	Stellar and Black Hole Masses	52
4.2.2.1	Galaxy and bulge stellar masses	54
4.2.2.2	Black hole mass estimates	56
4.2.3	Galaxy-Black Hole Mass Relations	57
4.2.4	Discussion	60

5	The influence of the group environment	63
5.1	Group Identification	63
5.1.1	Field sample	63
5.2	Results	66
5.3	Discussion	72
6	Discussion	76
7	Conlusions	78
	Bibliography	79

List of Figures

1.1	GZ2 classification decision tree	4
1.2	GZ2-GALEX sample completeness	5
1.3	Example SDSS images with GZ2 vote fractions	5
2.1	SFH models in observational planes	9
2.2	Predicted colours and SFRs of quenching models	11
2.3	Example STARPY output	14
2.4	Testing STARPY	15
2.5	Comparing complete and look-up table versions of STARPY	16
2.6	Colours of discarded galaxies	19
2.7	Replica colour-colour distributions using a hierarchical method	22
2.8	Replica colour-colour distributions using the POPSTARPY method	23
3.1	SFR-stellar mass plane split by morphology and colour	27
3.2	Population densities of red smooth and disc galaxies	29
3.3	Population densities of green smooth and disc galaxies	32
3.4	Population densities of blue smooth and disc galaxies	35
3.5	Best fit contours for red, green and blue clean galaxies	36
4.1	SDSS images of galaxies in the AGN-HOST sample	38
4.2	BPT diagram used to select AGN host galaxies	40
4.3	Colour-magnitude and SFR-mass diagram for AGN-HOST galaxies	42
4.4	Quenching time population density distributions for the AGN-HOST and INACTIVE samples	43
4.5	Quenching rate population density distributions for the AGN-HOST and INACTIVE samples	44
4.6	SDSS images of selected bulgeless, disc dominated galaxies	51
4.7	Optical spectra of 5 bulgeless galaxies observed on the INT with the IDS	53
4.8	Redshift distribution of bulgeless galaxies	54
4.9	Zoom in on $H\alpha$ region of the spectra of 5 galaxies observed with the IDS on the INT	58
4.10	Black hole bulge mass and stellar mass relations for the bulgeless AGN sample	59
4.11	Black hole mass against luminosity for the bulgeless AGN sample	61
4.12	Eddington ratio distribution of the bulgeless AGN sample	62

5.1	SDSS images of galaxies in the GZ-GROUP and GZ-FIELD samples	64
5.2	Redshift distribution comparison of the GZ-GROUP sample and matched control GZ-CENT-FIELD-Q sample	65
5.3	Mean GZ vote fractions for satellite galaxies with projected cluster centric radius	66
5.4	Bar fraction of satellite disc galaxies with projected cluster centric radius	67
5.5	Merger fraction of satellite galaxies with projected cluster centric radius	68
5.6	GZ2 bulge fractions of satellite disc galaxies with projected cluster centric radius	69
5.7	Median SFR of the GZ-GROUP sample with projected cluster centric radius	70
5.8	The time since quenching of the GZ-GROUP sample with projected cluster centric radius	73
5.9	The time since quenching of the GZ-GROUP sample with projected cluster centric radius	74

Chapter 1

Introduction

Previous large scale surveys of galaxies have revealed a bimodality in the colour-magnitude diagram (CMD) with two distinct populations; one at relatively low mass, with blue optical colours and another at relatively high mass, with red optical colours (Baldry et al., 2004, 2006; Willmer et al., 2006; Ball et al., 2008; Brammer et al., 2009). These populations were dubbed the ‘blue cloud’ and ‘red sequence’ respectively (Chester & Roberts, 1964; Bower et al., 1992; Driver et al., 2006; Faber et al., 2007). The Galaxy Zoo project (Lintott et al., 2011), which produced morphological classifications for a million galaxies, helped to confirm that this bimodality is not entirely morphology driven (Strateva et al., 2001; Salim et al., 2007; Schawinski et al., 2007; Constantin et al., 2008; Bamford et al., 2009; Skibba et al., 2009), detecting larger fractions of spiral galaxies in the red sequence (Masters et al., 2010a) and elliptical galaxies in the blue cloud (Schawinski et al., 2009) than had previously been detected.

The sparsely populated colour space between these two populations, the so-called ‘green valley’, provides clues to the nature and duration of galaxies’ transitions from blue to red. This transition must occur on rapid timescales, otherwise there would be an accumulation of galaxies residing in the green valley, rather than an accumulation in the red sequence as is observed (Arnouts et al., 2007; Martin et al., 2007). Green valley galaxies have therefore long been thought of as the ‘crossroads’ of galaxy evolution, a transition population between the two main galactic stages of the star forming blue cloud and the ‘dead’ red sequence (Bell et al., 2004; Wyder et al., 2007; Schiminovich et al., 2007; Martin et al., 2007; Faber et al., 2007; Mendez et al., 2011;

Gonçalves et al., 2012; Schawinski et al., 2014; Pan et al., 2014).

The intermediate colours of these green valley galaxies have been interpreted as evidence for recent quenching (suppression) of star formation (Salim et al., 2007). Star forming galaxies are observed to lie on a well defined mass-SFR relation, however quenching a galaxy causes it to depart from this relation (Noeske et al. 2007; Peng et al. 2010).

By studying the galaxies which have just left this mass-SFR relation, I can probe the quenching mechanisms by which this occurs. There have been many previous theories for the initial triggers of these quenching mechanisms, including negative feedback from AGN (Di Matteo et al., 2005; Martin et al., 2007; Nandra et al., 2007; Schawinski et al., 2007), mergers (Darg et al., 2010; Cheung et al., 2012; Barro et al., 2013), supernovae winds (Marasco et al., 2012), cluster interactions (Coil et al., 2008; Mendez et al., 2011; Fang et al., 2013) and secular evolution (Masters et al., 2010a, 2011; Mendez et al., 2011). By investigating the *amount* of quenching that has occurred in the blue cloud, green valley and red sequence; and by comparing the amount across these three populations, I can apply some constraints to these theories.

The nature of the observed co-evolution of galaxies and their central supermassive black holes (Magorrian et al., 1998; Marconi & Hunt, 2003; Häring & Rix, 2004) and the effects of AGN feedback on galaxies are two of the most important open issues in galaxy evolution. AGN feedback was first suggested as a mechanism for regulating star formation in simulations (Silk & Rees, 1998; Croton et al., 2006; Bower et al., 2006; Somerville et al., 2008) and indirect evidence has been observed for both positive and negative feedback in various systems (see the comprehensive review from Fabian 2012).

The strongest observational evidence for AGN feedback in a population is that the largest fraction of AGN are found in the green valley (Cowie & Barger, 2008; Hickox et al., 2009; Schawinski et al., 2010), suggesting some link between AGN activity and the process of quenching which moves a galaxy from the blue cloud to the red sequence. However, concrete statistical evidence for the effect of AGN feedback on the host galaxy population has so far been elusive.

There are many mechanisms which are proposed to cause quenching; including mergers (Daddi et al., 2010), mass quenching (Kennicutt et al., 1987; Peng et al., 2012), morphological quenching (?) and the environment of a galaxy.

The galaxy environment as a cause of quenching was proposed due to the correlation of both morphology (Dressler, 1980) and the quenched galaxy fraction (?) with environmental density.

BUT does this correlation truly imply causation? Evidence from simulations (?) suggests that the environment may not be the dominant quenching mechanisms for galaxies. Perhaps the correlation of increased galaxy quenched fractions with environment is due to a combination of mergers, mass and morphological quenching. In denser environments, galaxies are more likely to encounter another galaxy in a merger scenario and large viral radii give rise to long infall times during which gas reservoirs can be depleted due to star formation.

To study this I need to look at how quenching timescale changes in groups and clusters of galaxies with different properties in order to isolate the cause of the density-morphology and density-SFR correlations.

1.1 Galaxy Zoo

In this investigation I use visual classifications of galaxy morphologies from the Galaxy Zoo 2¹ citizen science project (Willett et al., 2013), which obtains multiple independent classifications for each galaxy image; the full question tree is shown in Figure 1.1.

The Galaxy Zoo 2 (GZ2) project consists of 304,022 images from the SDSS DR8 (a subset of those classified in Galaxy Zoo 1; GZ1) all classified by *at least* 17 independent users, with the mean number of classifications standing at ~ 42 . The GZ2 sample is more robust than the GZ1 sample and provides more detailed morphological classifications, including features such as bars, the number of spiral arms and the ellipticity of smooth galaxies. It is for these reasons I use the GZ2 sample, as opposed to the GZ1, allowing for further investigation of specific galaxy classes in the future.

The decision tree that users are led through whilst classifying galaxies with GZ2 is shown in Figure 1.1. The first task of GZ2 asks users to choose whether a galaxy is mostly smooth, is featured and/or has a disc or is a star/artefact. Unlike other tasks further down in the decision tree, every user who classifies a galaxy image will

¹<http://zoo2.galaxyzoo.org/>

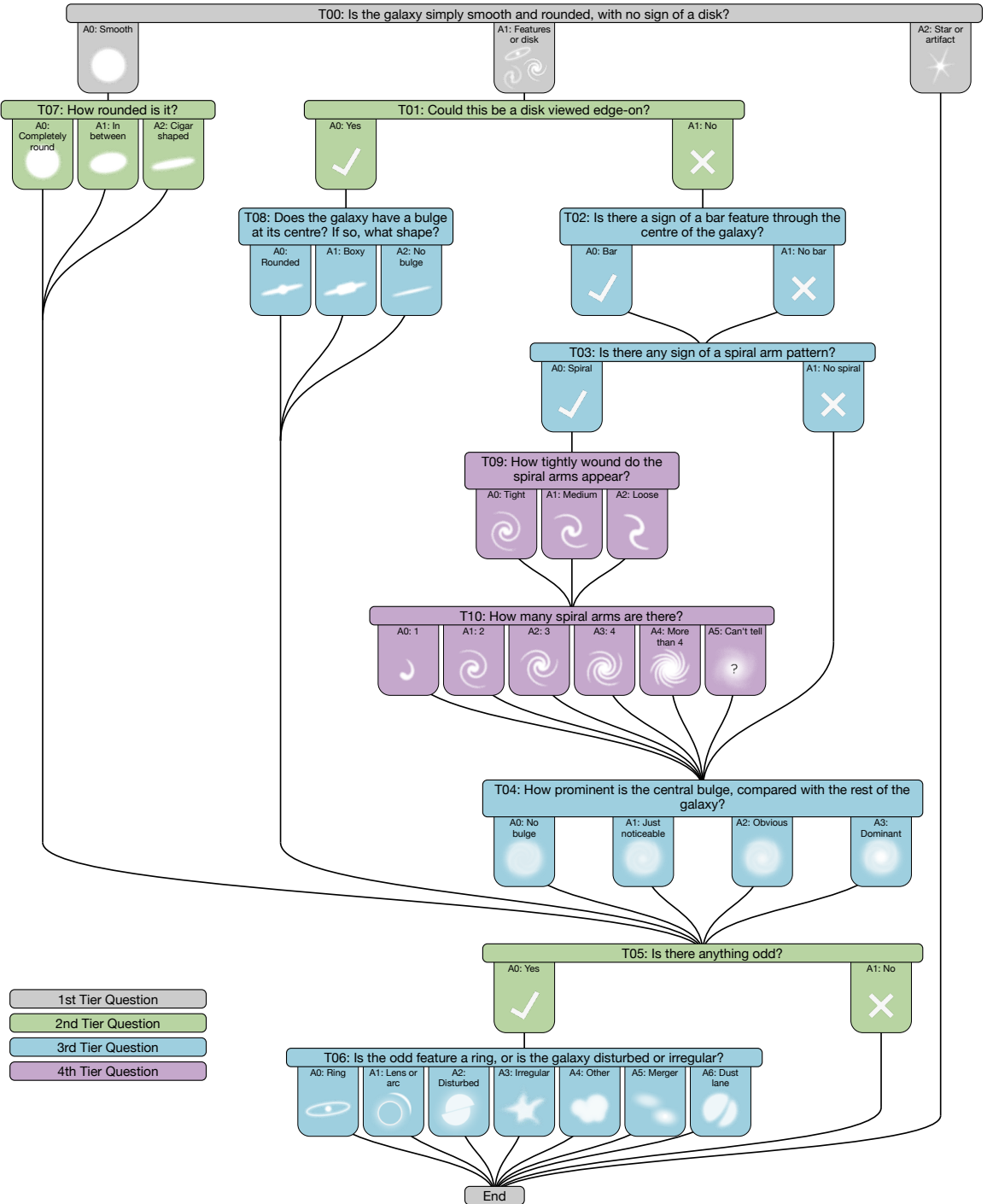


Figure 1.1: Flowchart of the classification tree for GZ2, beginning at the top. Tasks are colour-coded by their relative depths in the decision tree with tasks in green, blue and purple respectively one, two or three steps below branching points in the decision tree.

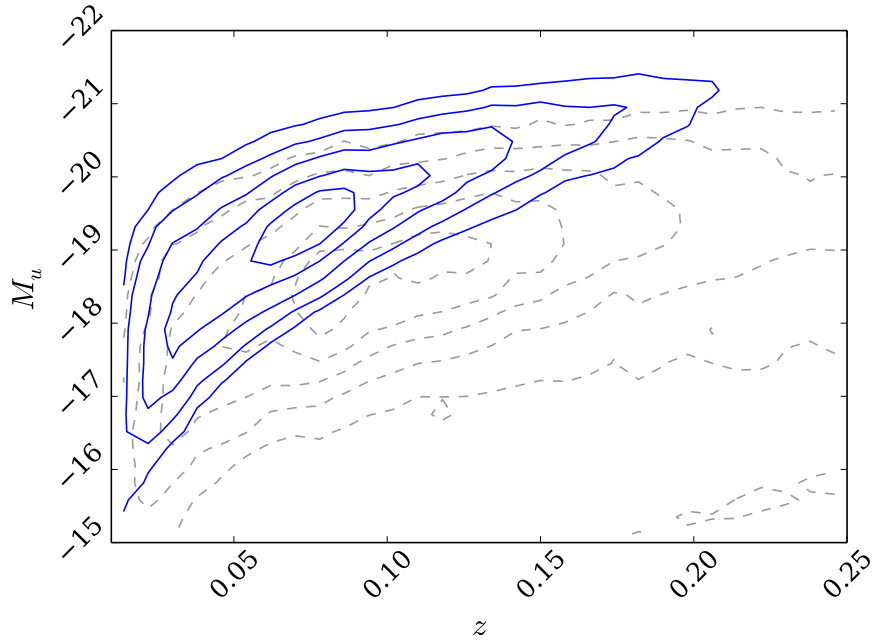


Figure 1.2: Absolute u -band magnitude against redshift for the whole of SDSS (grey dashed lines) in comparison to the GZ2 subsample (blue solid lines). Typical Milky Way L_* galaxies with $M_u \sim -20.5$ are still included in the GZ2 subsample out to the highest redshift of $z \sim 0.25$.

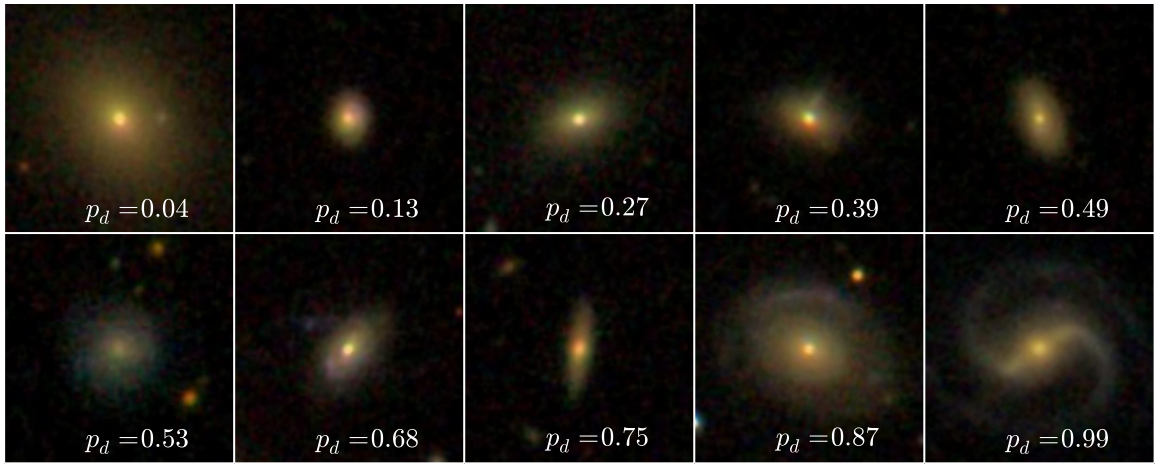


Figure 1.3: Randomly selected SDSS gri composite images showing the continuous probabilistic nature of the Galaxy Zoo sample from a redshift range $0.070 < z < 0.075$. The debiased disc vote fraction (see Willett et al. 2013) for each galaxy is shown. The scale for each image is 0.099 arcsec/pixel.

complete this task (others, such as whether the galaxy has a bar, is dependent on a user having first classified it as a featured galaxy). Therefore I have the most statistically robust classifications at this level.

The classifications from users produces a vote fraction for each galaxy (the debiased fractions calculated by Willett et al. (2013) were used in this investigation); for example if 80 of 100 people thought a galaxy was disc shaped, whereas 20 out of 100 people thought the same galaxy was smooth in shape (i.e. elliptical), that galaxy would have vote fractions $p_s = 0.2$ and $p_d = 0.8$. In this example this galaxy would be included in the ‘clean’ disc sample ($p_d \geq 0.8$) according to Willett et al. (2013) and would be considered a late-type galaxy. All previous Galaxy Zoo projects have incorporated extensive analysis of volunteer classifications to measure classification accuracy and bias, and compute user weightings (for a detailed description of debiasing and consistency-based user weightings, see either Section 3 of Lintott et al. 2009 or Section 3 of Willett et al. 2013).

The classifications are highly accurate and provide a continuous spectrum of morphological features, as shown in Figure 4.1, rather than a simple binary classification separating elliptical and disc galaxies. These classifications allow each galaxy to be considered as a probabilistic object with both bulge and disc components.

1.1.1 Defining the `gz2-galex` main galaxy sample

The only selection that was made on the GZ2 sample was to remove objects considered to be stars, artefacts or merging pairs by the users (i.e. with $p_{\text{star/artefact}} \geq 0.8$ or $p_{\text{merger}} \geq 0.420$; see Willett et al. 2013 Table 3 and discussion for details of this fractional limit). Further to this, I required NUV photometry from the GALEX survey, within which $\sim 42\%$ of the GZ2 sample were observed, giving a total sample size of 126,316 galaxies. This will be referred to as the `gz2-GALEX` sample.

The completeness of the `gz2-GALEX` sample is shown in Figure 1.2 with the u -band absolute magnitude against redshift, compared with the SDSS data set. Typical Milky Way L_* galaxies with $M_u \sim -20.5$ are still included in the GZ2 subsample out to the highest redshift of $z \sim 0.25$; however dwarf and lower mass galaxies are only detected at the lowest redshifts.

Chapter 2

STARPY: Bayesian inference of a galaxy's star formation history

The work in the following chapter has been published in Smethurst et al. (2015).

2.1 Star Formation History Models

The quenched star formation history (SFH) of a galaxy can be simply modelled as an exponentially declining star formation rate (SFR) across cosmic time ($0 \leq t$ [Gyr] ≤ 13.8) as:

$$SFR = \begin{cases} I_{sfr}(t_q) & \text{if } t < t_q \\ I_{sfr}(t_q) \times \exp\left(\frac{-(t-t_q)}{\tau}\right) & \text{if } t > t_q \end{cases} \quad (2.1)$$

where t_q is the onset time of quenching, τ is the timescale over which the quenching occurs and I_{sfr} is an initial constant star formation rate dependent on t_q . A smaller τ value corresponds to a rapid quench, whereas a larger τ value corresponds to a slower quench.

Here I assume that all galaxies formed at a time $t = 0$ Gyr with an initial burst of star formation. The mass of this initial burst is controlled by the value of the I_{sfr} which is set as the average specific SFR (sSFR) at the time of quenching t_q . Peng et al. (2010) defined a relation (their equation 1) between the average sSFR and redshift (cosmic time, t) by fitting to measurements of the mean sSFR of blue star

forming galaxies from SDSS, zCOSMOS and literature values at increasing redshifts (Elbaz et al., 2007; Daddi et al., 2007):

$$sSFR(m, t) = 2.5 \left(\frac{m}{10^{10} M_{\odot}} \right)^{-0.1} \left(\frac{t}{3.5 \text{ Gyr}} \right)^{-2.2} \text{Gyr}^{-1}. \quad (2.2)$$

Beyond $z \sim 2$ the characteristic SFR flattens and is roughly constant back to $z \sim 6$. The cause for this change is not well understood but can be seen across similar observational data (Peng et al., 2010; González et al., 2010; Béthermin et al., 2012). Motivated by these observations, the relation defined in Peng et al. (2010) is taken up to a cosmic time of $t = 3$ Gyr ($z \sim 2.3$) and prior to this a constant average SFR is assumed (see middle panel of Figure 2.1). At the point of quenching, t_q , the SFH models are defined to have an I_{sfr} which lies on this relationship for the sSFR, for a galaxy with mass, $m = 10^{10.27} M_{\odot}$ (the mean mass of the GZ2-GALEX sample; see left panel of Figure 2.1).

Under these assumptions the average SFR of these models will result in a lower value than the relation defined in Peng et al. (2010) at all cosmic times as each galaxy only resides on the ‘main sequence’ at the point of quenching. However galaxies cannot remain on the ‘main sequence’ from early to late times throughout their entire lifetimes given the unphysical stellar masses and SFRs this would result in at the current epoch in the local Universe (Béthermin et al., 2012; Heinis et al., 2014). If prescriptions for starbursts, mergers, AGN etc. were included in this model, the reproduction of the average SFR across cosmic time would improve; however I have chosen to first focus on the simplest possible model.

Once this evolutionary SFR is obtained, it is convolved with the Bruzual & Charlot (2003) population synthesis models to generate a model SED at each time step. The observed features of galaxy spectra can be modelled using simple stellar population techniques which sum the contributions of individual, coeval, equal-metallicity stars. The accuracy of these predictions depends on the completeness of the input stellar physics. Comprehensive knowledge is therefore required of (i) stellar evolutionary tracks and (ii) the initial mass function (IMF) to synthesise a stellar population accurately.

These stellar population synthesis (SPS) models are an extremely well explored (and often debated) area of astrophysics (Maraston, 2005; Eminian et al., 2008; Conroy et al., 2009; Falkenberg et al., 2009; Chen et al., 2010; Kriek et al., 2010; Miner et al., 2011; Melbourne et al., 2012). In this work I have chosen to utilise the Bruzual

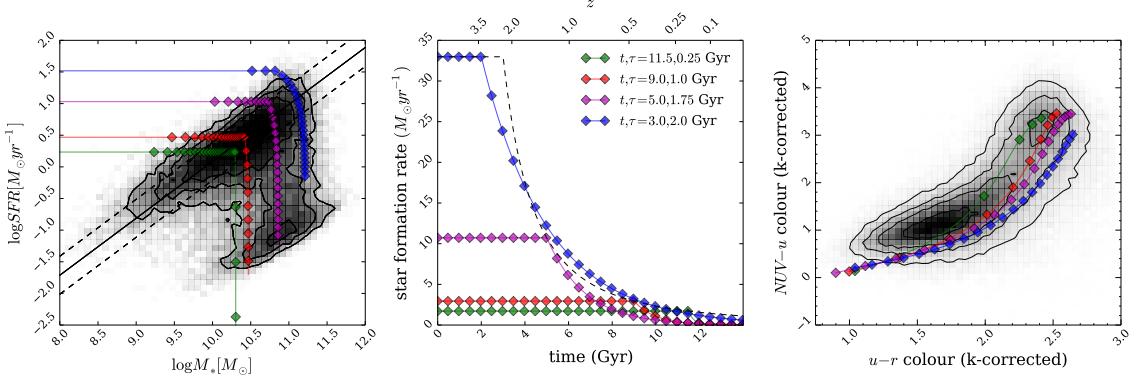


Figure 2.1: Left panel: SFR-stellar mass plane for all 126,316 galaxies in the GZ2-GALEX sample (shaded contours), with model galaxy trajectories shown by the coloured lines, with each point representing a time step of 0.5 Gyr. The ‘main sequence’ of star formation as defined by Peng et al. (2010) is shown by the solid line with $\pm 1\sigma$ (dashed lines). Middle panel: The SFHs of the models are shown, where the SFR is initially constant before quenching at time t_q and thereafter exponentially declining with a characteristic timescale τ . The SFR at the point of quenching is set to be consistent with the typical SFR of a star-forming galaxy at the quenching time, t_q (dashed curve; Peng et al. 2010). Right panel: The full range of models can reproduce the observed colour-colour properties of the sample; for clarity the figures show only 4 of the possible models explored in this study. Note that some of the model tracks produce colours redder than the apparent peak of the red sequence in the GZ2 subsample; however this is not the *true* peak of the red sequence due to the necessity for NUV colours from GALEX.

& Charlot (2003) *GALExEV* SPS models, along with a Chabrier IMF (Chabrier, 2003), across a large wavelength range ($0.0091 < \lambda [\mu\text{m}] < 160$) with solar metallicity (m62 in the Bruzual & Charlot (2003) models; hereafter BC03), to allow a direct comparison with Schawinski et al. (2014).

Fluxes from stars younger than 3 Myr in the SPS model are suppressed to mimic the large optical depth of protostars embedded in dusty formation clouds (as in Schawinski et al. 2014). Filter transmission curves are then applied to the fluxes to obtain AB magnitudes and ultimately colours. For a particular galaxy at an observed redshift, z , I calculate the observed time, t^{obs} for that galaxy using the standard cosmological conversion between redshift and time provided in the *ASTROPY Python* module (Astropy Collaboration et al., 2013). The predicted colours of the SFH models at the observed redshift of each individual galaxy can then be compared to the observed colours directly.

Figure 2.2 shows these predicted optical and NUV colours at a time of $t^{obs} = 12.8$ Gyr (the average observed time of the GZ2-GALEX sample, $z \sim 0.076$) for the exponential SFH model. These predicted colours will be referred to as $d_{c,p}(t_q, \tau, t^{obs})$, where $c=\{\text{opt,NUV}\}$ and $p = \text{predicted}$. The SFR at a time of $t^{obs} = 12.8$ Gyr is also shown in Figure 2.2 to compare how this correlates with the predicted colours. The $u - r$ predicted colour shows an immediate correlation with the SFR, however the $NUV - u$ colour is more sensitive to the value of τ and so is ideal for tracing any recent star formation in a population. At small τ (rapid quenching timescales) the $NUV - u$ colour is insensitive to t_q , whereas at large τ (slow quenching timescales) the colour is very sensitive to t_q . Together the two colours are ideal for tracing the effects of t_q and τ in a population.

This model is not a fully hydrodynamical simulation, it is a simple model built in order to test our understanding of the evolution of galaxy populations. These models are therefore not expected to accurately determine the SFH of every galaxy in the GZ2-GALEX sample, in particular galaxies which have not undergone any quenching. In this case the models described above can only attribute a constant star formation rate to these unquenched galaxies. In reality, there are many possible forms of SFH that a galaxy can take, a few of which have been investigated in previous literature; starbursts (Canalizo & Stockton, 2001), a power law (Glazebrook et al., 2003), single stellar populations (Trager et al., 2000; Sánchez-Blázquez et al., 2006; Vazdekis et al., 2010), log-normal distributions (Abramson et al., 2016) and metallicity enrichment

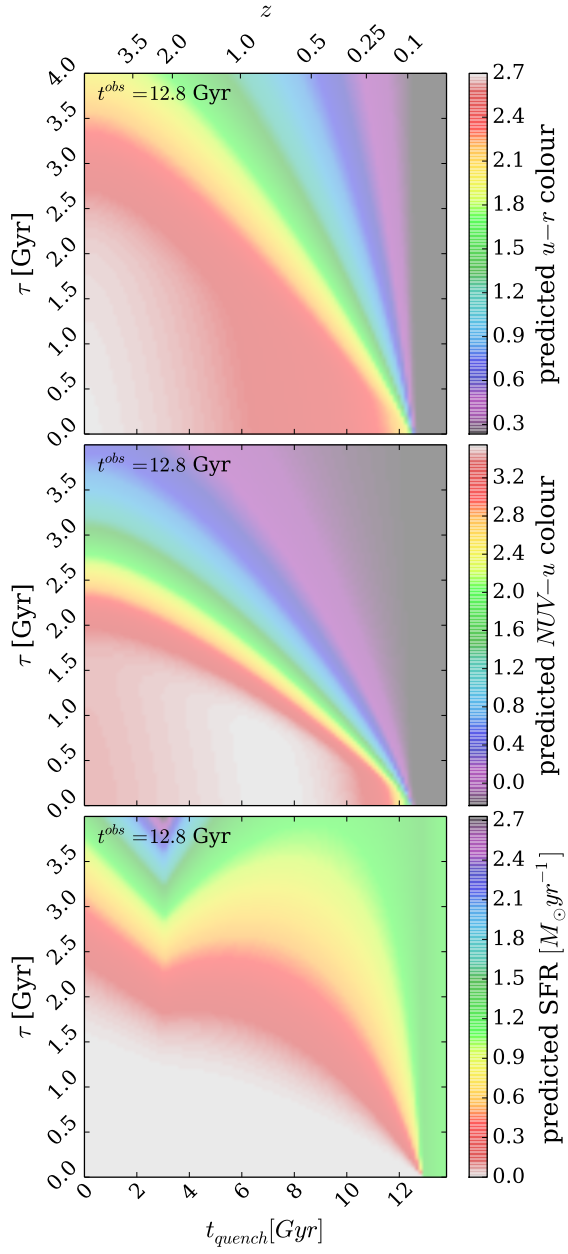


Figure 2.2: Quenching timescale τ versus quenching onset time t_q in all three panels for the quenched SFH models used in STARPY. Colour shadings show model predictions of the $u - r$ optical colour (top panel), $NUV - u$ colour (middle panel), and star formation rate (lower panel), at $t^{\text{obs}} = 12.8 \text{ Gyr}$, the mean observed redshift of the GZ2 sample (see Section 2.1). The combination of optical and NUV colours is a sensitive measure of the $\theta = [t_q, \tau]$ parameter space. Note that all models with $t > 12.8 \text{ Gyr}$ are effectively un-quenched. The ‘kink’ in the bottom panel is due to the assumption that the sSFR is constant prior to $t \sim 3 \text{ Gyr}$ ($z \sim 2.2$).

(De Lucia et al., 2014). Incorporating these different SFHs along with prescriptions for mergers and a possible reinvigoration of star formation post quench (e.g. see recent work by Pontzen et al. 2016) into the SFH models is a possible future extension to this work once the results of this study are well enough understood to permit additional complexity to be added.

2.2 Probabilistic Fitting Methods

In order to achieve robust conclusions I conducted a Bayesian analysis (Sivia & Skilling, 2006; Mackay, 2003) of the predicted colours from the SFH models in comparison to the observed colours of the GZ2-GALEX sample. This approach requires consideration of all possible combinations of $\theta \equiv (t_q, \tau)$. Assuming that all galaxies formed at $t = 0$ Gyr with an initial burst of star formation, we can assume that the ‘age’ of each galaxy in the GZ2 sample is equivalent to an observed time, t_k^{obs} . I then used this ‘age’ to calculate the predicted model colours at this cosmic time for a given combination of θ : $d_{c,p}(\theta_k, t_k^{obs})$ for both optical and NUV ($c = opt, NUV$) colours. The predicted model colours can now directly be compared with the observed GZ2-GALEX sample colours, so that for a single galaxy k with optical ($u - r$) colour, $d_{opt,k}$ and NUV ($NUV - u$) colour, $d_{NUV,k}$, the likelihood of a given model $P(d_k|\theta_k, t_k^{obs})$ is:

$$P(d_k|\theta_k, t_k^{obs}) = \frac{1}{\sqrt{2\pi\sigma_{opt,k}^2}} \frac{1}{\sqrt{2\pi\sigma_{NUV,k}^2}} \exp \left[-\frac{(d_{opt,k} - d_{opt,p}(\theta_k, t_k^{obs}))^2}{\sigma_{opt,k}^2} \right] \\ \exp \left[-\frac{(d_{NUV,k} - d_{NUV,p}(\theta_k, t_k^{obs}))^2}{\sigma_{NUV,k}^2} \right]. \quad (2.3)$$

Here I have assumed that $P(d_{opt}|\theta_k, t_k^{obs})$ and $P(d_{NUV}|\theta_k, t_k^{obs})$ are independent of each other and that the errors on the observed colours are also independent. To obtain the probability of a combination of θ values given the GZ2 data: $P(\theta_k|d_k, t^{obs})$, i.e. how likely is a single SFH model given the observed colours of a single GZ2 galaxy, I utilise Bayes’ theorem:

$$P(\theta_k|d_k, t^{obs}) = \frac{P(d_k|\theta_k, t^{obs})P(\theta_k)}{\int P(d_k|\theta_k, t^{obs})P(\theta_k)d\theta_k}. \quad (2.4)$$

I assume a flat prior on the model parameters so that:

$$P(\theta_k) = \begin{cases} 1 & \text{if } 0 \leq t_q \text{ [Gyr]} \leq 13.8 \text{ and } 0 \leq \tau \text{ [Gyr]} \leq 4 \\ 0 & \text{otherwise.} \end{cases} \quad (2.5)$$

As the denominator of Equation 2.4 is a normalisation factor, comparison between likelihoods for two different SFH models (i.e., two different combinations of $\theta_k = [t_q, \tau]$) is equivalent to a comparison of the numerators. Markov Chain Monte Carlo (MCMC; Mackay 2003; Foreman-Mackey et al. 2013; Goodman & Weare 2010) provides a robust comparison of the likelihoods between θ values; here I choose *emcee*,¹ a Python implementation of an affine invariant ensemble sampler by Foreman-Mackey et al. (2013).

This method allows for a more efficient exploration of the parameter space by avoiding those areas with low likelihood. A large number of ‘walkers’ are started at an initial position where the likelihood is calculated; from there they individually ‘jump’ to a new area of parameter space. If the likelihood in this new area is greater (less) than the original position then the ‘walkers’ accept (reject) this change in position. Any new position then influences the direction of the ‘jumps’ of other walkers. This is repeated for the defined number of steps after an initial ‘burn-in’ phase. *emcee* returns the positions of these ‘walkers’, which are analogous to the regions of high probability in the model parameter space.

The routine outlined above has been coded using the *Python* programming language into a package named STARPY which has been made freely available to download². An example output from this module for a single galaxy from the GZ2-GALEX sample in the red sequence is shown in Figure 2.2.

2.3 Testing STARPY

In order to test that STARPY can find the correct quenching model for a given observed colour, 25 synthesised galaxies were created with known SFHs (i.e. known values of $\theta = [t_q, \tau]$) from which optical and NUV colours were generated using the BC03 SPS models. These were input into STARPY to test whether the known values of θ were

¹[emcee13.iel.fm/emcee/](https://github.com/ielfm/emcee/)

²github.com/zooniverse/starpyp

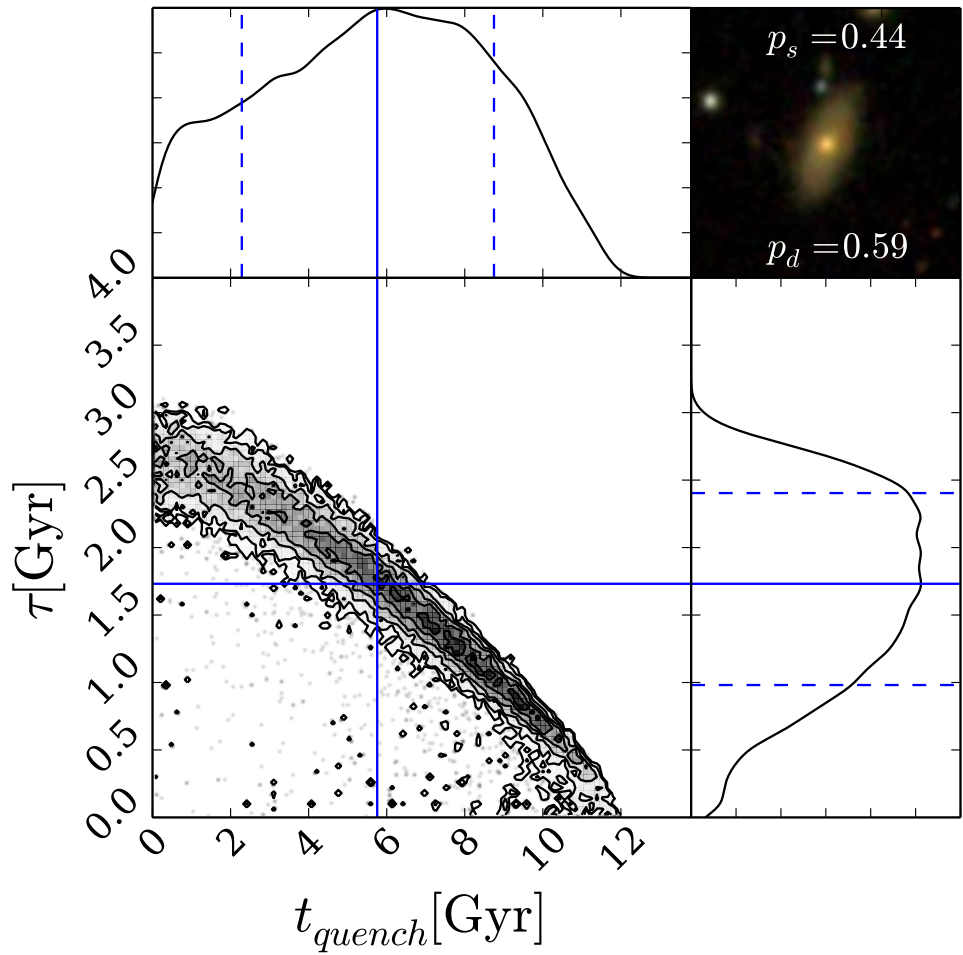


Figure 2.3: Example output from STARPY for a galaxy within the red sequence. The contours show the positions of the ‘walkers’ in the Markov Chain (which are analogous to the areas of high probability) for the quenching models described by $\theta = [t_q, \tau]$. The histograms show the 1D projection along each axis. Solid (dashed) blue lines show the best fit parameters (with $\pm 1\sigma$) to the data. The postage stamp image from SDSS is shown in the top right along with the debiased vote fractions for smooth (p_s) and disc (p_d) from Galaxy Zoo 2.

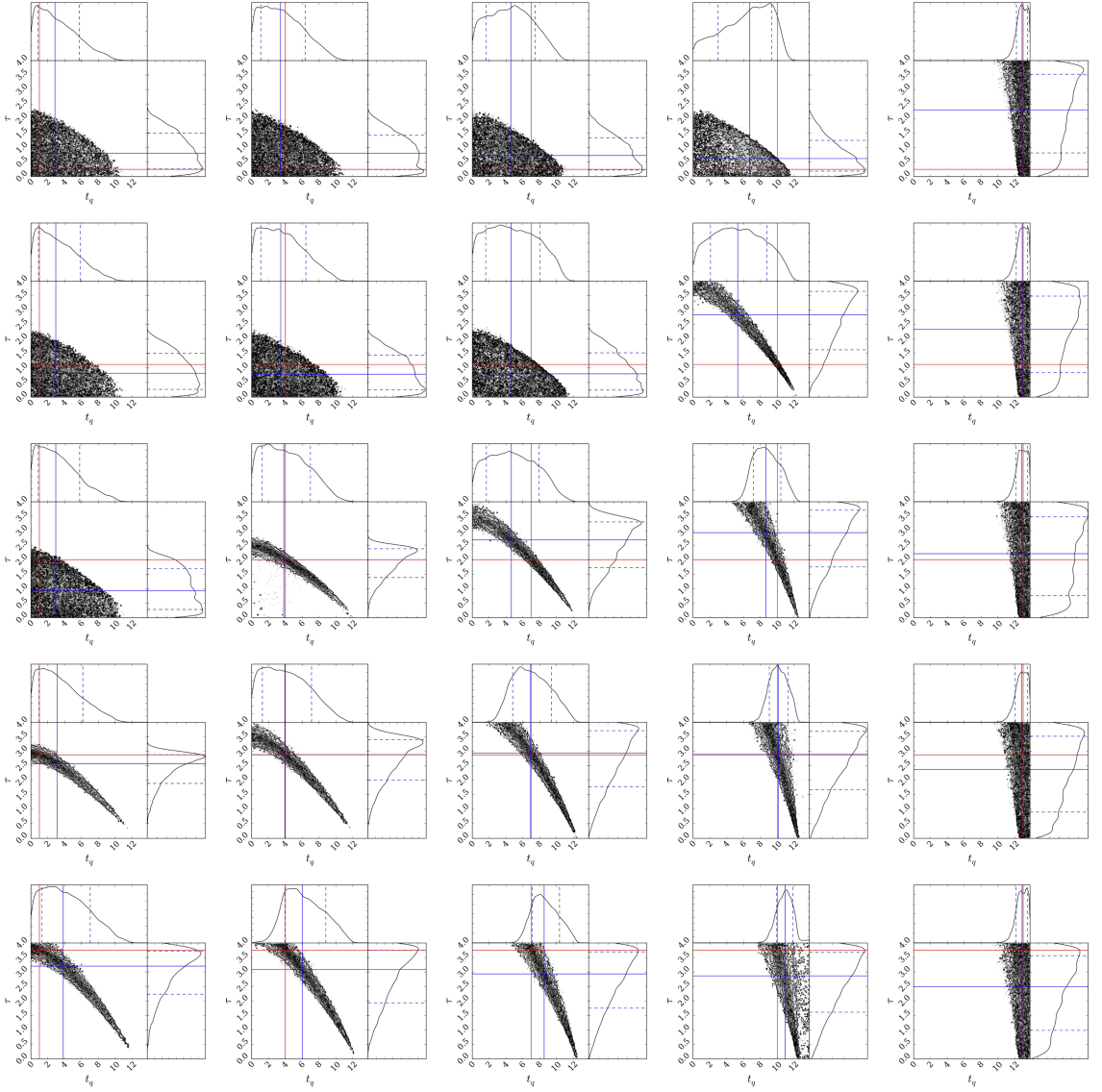


Figure 2.4: Results from STARPY for an array of synthesised galaxies with known, i.e. true, t_q and τ values (marked by the red lines) using the complete function to calculate the predicted colour of a proposed set of θ values in each MCMC iteration, assuming an error on the calculated known colours of $\sigma_{u-r} = 0.124$ and $\sigma_{NUV-u} = 0.215$ (the average errors on the GZ sample colours). I also assume that each synthesised galaxy has been observed at a redshift of $z = 0$. In each case STARPY succeeds (50th percentile best fit parameters are shown by the blue lines) in locating the true parameter values within the degeneracies of the star formation history model.

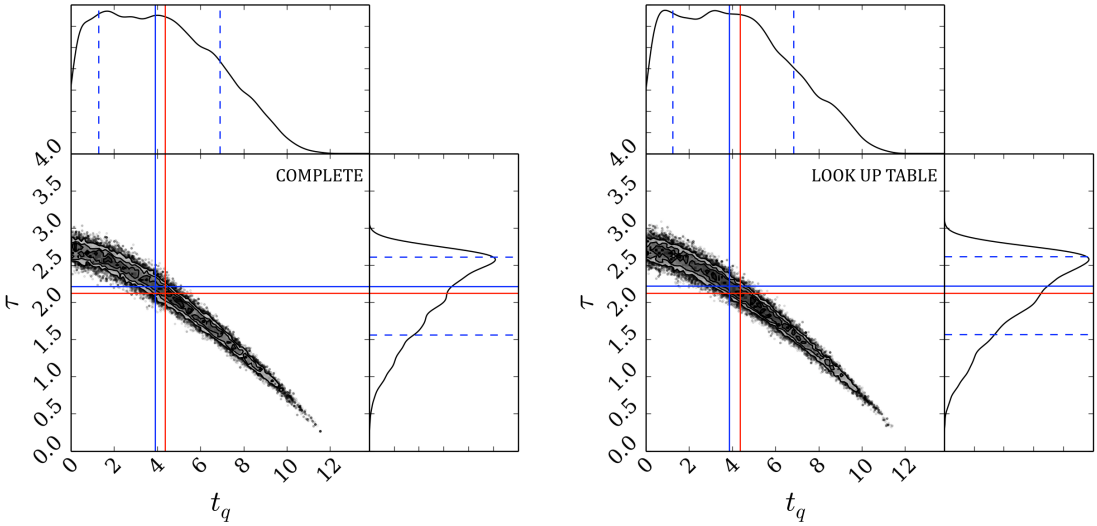


Figure 2.5: Left panel: Results from STARPY for true t_q and τ values (red lines) using the complete function to calculate the predicted colour of a proposed set of θ values in each MCMC iteration. The median walker position (the 50th percentile of the Bayesian probability distribution) is shown by the solid blue line with the dashed lines encompassing 68%($\pm 1\sigma$) of the samples (the 16th and 84th percentile positions). The time taken to run for a single galaxy using this method is approximately 2 hours. Right panel: Results from STARPY for true t_q and τ values using a look up table generated from the complete function to calculate the predicted colour of a proposed set of θ values in each MCMC iteration. The time taken to run for a single galaxy using this method is approximately 2 minutes.

reproduced, within error, for each of the 25 synthesised galaxies. Figure 2.4 shows the results for each of these synthesised galaxies, with the known values of θ shown by the red lines. In some cases this red line does not coincide with the inferred best fit θ values shown by the blue lines, however in all cases the intersection of the red lines is within the sample contours; therefore STARPY succeeds in locating the true parameter values within the degeneracies of the SFH model.

2.4 Speeding up STARPY

I wish to consider the SFH model parameters for a large populations of galaxies across the colour magnitude diagram, however for each combination of θ values which *emcee*

Table 2.1: Median walker positions (the 50th percentile; as shown by the blue solid lines in Figure 2.5) found by STARPY for a single galaxy, using the complete star formation history function and a look up table to speed up the run time. The errors quoted define the region in which 68% of the samples are located, shown by the dashed blue lines in Figure 2.5. The known true values are also quoted, as shown by the red lines in Figure 2.5. All values are quoted to three significant figures.

	t_q	τ
True	4.37	2.12
Complete	$3.893 \pm^{3.014}_{2.622}$	$2.215 \pm^{0.395}_{0.652}$
Look up table	$3.850 \pm^{2.988}_{2.619}$	$2.218 \pm^{0.399}_{0.649}$

proposes for a single galaxy, a new SFH must be built, prior to convolving it with the BC03 SPS models at the observed age and then predicted colours calculated from the resultant SED. For a single galaxy this takes up to 2 hours on a typical desktop machine for long Markov Chains. A 3-dimensional look-up table was therefore generated at 50 t^{obs} , 100 t_{quench} and 100 τ values; this was then interpolated over for a given observed galaxy’s age and proposed θ values at each step in the Markov Chain. This ensured that a single galaxy takes approximately 2 minutes to run on a typical desktop machine.

Figure 2.5 shows an example of how using the look up table in place of the full function does not affect the results to a significant level. Table 2.4 quotes the median walker positions (the 50th percentile of the Bayesian probability distribution) along with their $\pm 1\sigma$ ranges for both methods in comparison to the true values specified to test STARPY. The uncertainties incorporated into the quoted values by using the look up table are therefore minimal with a maximum $\Delta = 0.043$.

Using this lookup table, each of the 126,316 total galaxies in the GZ2-GALEX sample was run through STARPY on multiple cores of a computer cluster to obtain the Markov Chain positions (analogous to $P(\theta_k|d_k)$) for each galaxy, k (see Figure 2.2). In each case the Markov Chain consisted of 100 ‘walkers’ which took 400 steps in the ‘burn-in’ phase and 400 steps thereafter, at which point the MCMC acceptance fraction was checked to be within the range $0.25 < f_{acc} < 0.5$ (which was true in all cases). Due to the Bayesian nature of this method, a statistical test on the results is not possible; the output is probabilistic in nature across the entirety of the parameter space.

2.5 POPSTARPY: studying populations of galaxies with STARPY

To study the SFH of a large population of galaxies, the individual galaxy walker positions output by STARPY (analogous to the posterior probability distribution) are combined across $[t, \tau]$ space. The Markov Chain walker positions are binned and weighted by their corresponding logarithmic posterior probability $\log[P(\theta_k|d_k)]$, provided by the *emcee* package, in order to emphasise the features and differences between various populations. This weighting by $\log[P(\theta_k|d_k)]$ is to minimise the contribution of galaxies poorly fit by this exponentially declining SFH. This is no longer inference but merely a method to visualise the results across a population of galaxies.

I also discard those walker positions with a corresponding normalised posterior probability of $P(\theta_k|d_k) < 0.2$ in order to exclude galaxies which are not well fit by the quenching model, therefore galaxies in each sample which reside on the main sequence will not contribute to the final population distribution of quenching parameters. This raises the issue of whether I exclude a significant fraction of the GZ2-GALEX sample and whether those galaxies reside in a specific location of the colour-magnitude. The fraction of galaxies which had all or more than half of their walker positions discarded due to low probability are shown in Table 2.5. Using the $P(\theta_k|d_k) < 0.2$ constraint, 2.4%, 7.0% and 5.4% of green, red and blue galaxies respectively had *all* of their walker positions discarded.

This is not a significant fraction of either population, therefore the STARPY module is effective in fitting the majority of galaxies and this method of discarding walker positions ensures that poorly fit galaxies are removed from the analysis of the results. Figure 2.6 shows that these galaxies with discarded walker positions are also scattered across the optical-NUV colour-colour diagram and therefore STARPY is also effective in fitting galaxies across this entire plane.

Figure 2.4 shows how peaks in the histograms are found across all areas of the parameter space in both dimensions $[t, \tau]$, ensuring that any conclusions drawn from combined population distributions are due to a superposition of extended probability distributions, as opposed to a bimodal distribution of probability distributions across all galaxies.

Table 2.2: The number of galaxies in each population which had walker positions discarded due to low posterior probability values in order to exclude those galaxies from the analysis which were poorly fit by the SFH quenching model.

	Red Sequence	Green Valley	Blue Cloud
All walkers discarded	1420 (7.00%)	437 (2.41%)	3109 (5.37%)
More than half walker positions discarded	2010 (9.92%)	779 (4.30%)	6669 (11.52%)

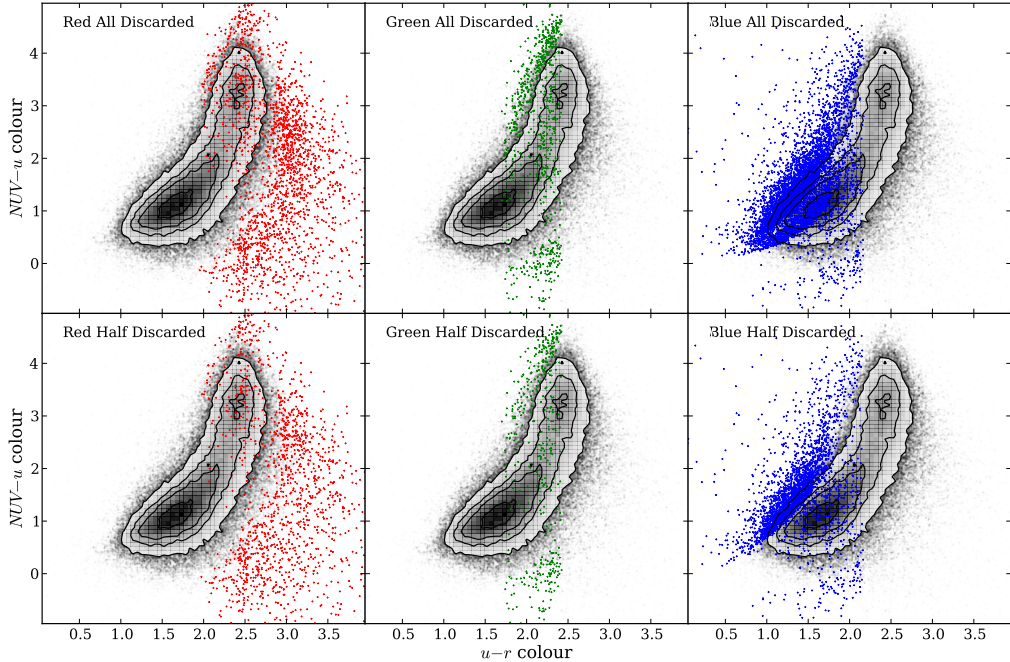


Figure 2.6: Contours show the full GZ2 subsample optical-NUV colour-colour diagram. The points show the positions of the galaxies which had all (top panels) or more than half (bottom panel) of their walker positions discarded due to their low probability for the red sequence (left), green valley (middle) and blue cloud (right).

The classifications from Galaxy Zoo 2 provide a uniquely powerful continuous measurements of a galaxy’s morphology, therefore I utilise the debiased user vote fractions to obtain separate population density distributions for both smooth and disc galaxies. This is obtained by also weighting by the morphology vote fraction when the binned walker positions are combined. This ensures that the entirety of the population is used, with galaxies with a higher p_d contributing more to the disc weighted than the smooth weighted population distribution. This negates the need for a threshold on the GZ2 vote fractions (e.g., $p_d > 0.8$ as used in Schawinski et al., 2014). These distributions will be referred to as the population densities.

For example, the galaxy shown in Figure 2.2 would contribute almost evenly to both the smooth and disc parameters due to the GZ2 vote fractions. Since galaxies with similar vote fractions contain both a bulge and disc component, this method is effective in incorporating intermediate galaxies which are thought to be crucial to the morphological changes between early- and late-type galaxies. It was the consideration of these intermediate galaxies which was excluded from the investigation by Schawinski et al. (2014).

2.5.1 Alternative Hierarchical Bayesian approach

The approach presented above relies upon a visualisation of the SFHs across each population, with no inference involved beyond the use of STARPY to derive the individual galaxy SFHs. An alternative approach to this problem would be to use a hierarchical Bayesian method to determine the ‘hyper-parameters’ that describe the distribution of the parent population $\theta' = [t'_q, \tau']$ that each individual galaxy’s SFH is drawn from.

The posterior PDF for $\vec{\theta}'$ to describe such a galaxy population:

$$P(\vec{\theta}'|\vec{d}) = \frac{P(\vec{d}|\vec{\theta}')P(\vec{\theta}')}{P(\vec{d})}, \quad (2.6)$$

where \vec{d} represents all of the optical and NUV colour data in a population $\{\vec{d}_k\}$. For one galaxy, k , the marginalised likelihood is:

$$P(d_k|\vec{\theta}') = \iint P(d_k|t_k, \tau_k)P(t_k, \tau_k|\vec{\theta}') \, dt_k \, d\tau_k \quad (2.7)$$

and for all galaxies, N , therefore:

$$P(\vec{d}|\vec{\theta}') = \prod_k^N P(d_k|\vec{\theta}'). \quad (2.8)$$

Using STARPY for an individual galaxy, k the output is the ‘interim’ posterior $P(t_k, \tau_k|d_k)$ which I can relate to $P(d_k|t_k, \tau_k)$ so that:

$$P(d_k|\vec{\theta}') = \iint P(t_k, \tau_k|d_k) \cdot P(d_k) \cdot \frac{P(t_k, \tau_k|\vec{\theta}')}{P(t_k, \tau_k)} dt_k d\tau_k. \quad (2.9)$$

In order to calculate this I draw N_s random samples, r , from each interim posterior, $P(t_k, \tau_k|d_k)$ so that Equation 2.9 can be expressed as a sum over a number of random samples, N_s (as with the calculation of an expected mean):

$$P(d_k|\vec{\theta}') = \frac{P(d_k)}{N_s} \sum_r^{N_s} \frac{P(t_{k,r}, \tau_{k,r}|\vec{\theta}')}{P(t_k, \tau_k)}, \quad (2.10)$$

for the r^{th} sample of N_s total samples taken from one galaxy’s, k , interim posterior PDF. This fraction is known as the ‘importance weight’, w_r , in importance sampling.

However, I also have two morphological vote fractions that I can weight by to determine separate hyper-parameters, $\vec{\theta}' = [\vec{\theta}_d', \vec{\theta}_s']$, for both disc, d , and smooth, s , galaxies. Therefore:

$$w_r = \frac{P(t_{k,r}, \tau_{k,r}|\vec{\theta}')}{P(t_k, \tau_k)} = \frac{p_{d,k}P(t_{k,r}, \tau_{k,r}|\vec{\theta}_d') + p_{s,k}P(t_{k,r}, \tau_{k,r}|\vec{\theta}_s')}{P(t_k, \tau_k)} \quad (2.11)$$

If we substitute equation 2.10 into equation 2.6 we find that the $P(d_k)$ terms cancel and we are left with:

$$P(\vec{\theta}'|\vec{d}) = P(\vec{\theta}') \prod_k^N \frac{1}{N_{s,k}} \sum_r^{N_s} w_r, \quad (2.12)$$

where $P(\vec{\theta}')$ is the assumed prior on the hyper-parameters, which is assumed to be uniform.

This approach is heavily dependent on what shape is assumed for the hyper-distribution; a decision which is not trivial. It is often common for this function to take the form of a multi-component Gaussian mixture model (Mackay, 2003;

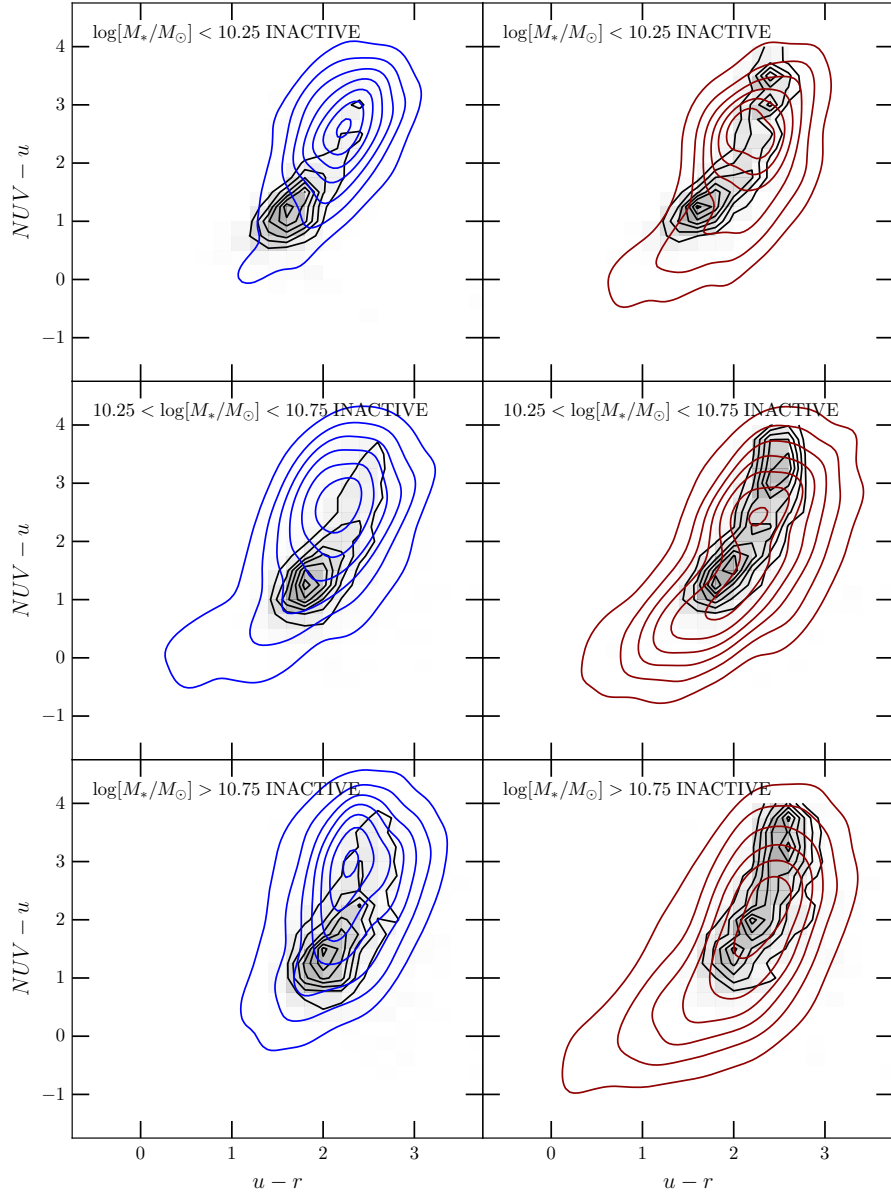


Figure 2.7: Optical-NUV colour-colour diagrams for the INACTIVE galaxies shown by the black contours, split into low mass (top), medium mass (middle) and high mass (bottom) galaxies weighted by p_d (left) and p_s (right). Kernel smoothing has been applied to the overlaid replica datasets, which are created by sampling from the **inferred 2 component Gaussian mixture model hierarchical parent distributions**. Gaussian random noise is also added to the inferred colours, with a mean and standard deviation of the errors on the observed colours of the respective sample. Contours are shown for samples taken from the disc (blue) and smooth weighted (red) inferred hierarchical distributions.

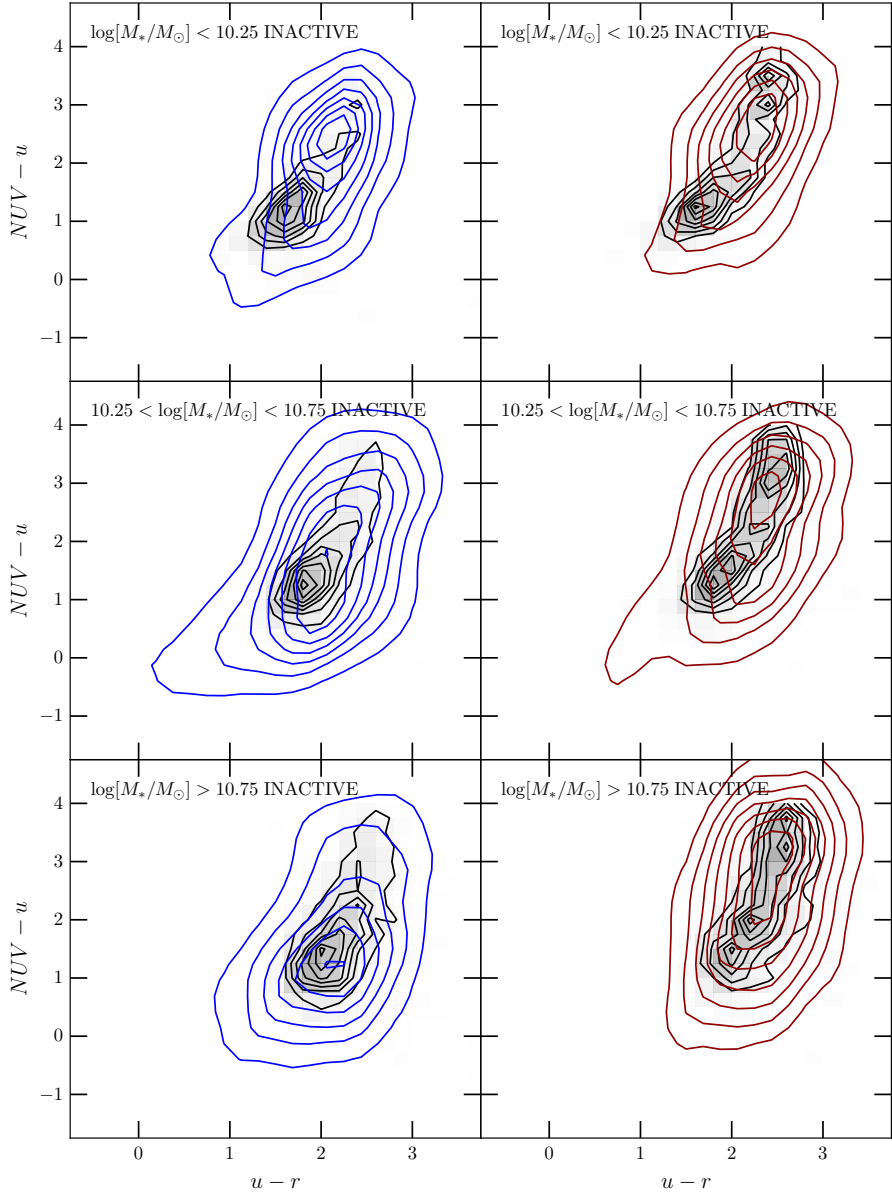


Figure 2.8: Optical-NUV colour-colour diagrams for the INACTIVE galaxies shown by the black contours, split into low mass (top), medium mass (middle) and high mass (bottom) galaxies weighted by p_d (left) and p_s (right). Kernel smoothing has been applied to the overlaid replica datasets, which are created by sampling from the **popstarpy population density distributions described in Section 2.5**. Gaussian random noise is also added to the inferred colours, with a mean and standard deviation of the errors on the observed colours of the respective sample. Contours are shown for samples taken from the disc (blue) and smooth weighted (red) inferred hierarchical distributions.

Lahav et al., 2000). For example a two component Gaussian mixture model in $[t, \tau]$ space is described by eight hyper-parameters for a single morphology, $\vec{\theta}' = [\mu_{t,1}, \sigma_{t,1}, \mu_{\tau,1}, \sigma_{\tau,1}, \mu_{t,2}, \sigma_{t,2}, \mu_{\tau,2}, \sigma_{\tau,2}]$. This approach assumes no covariance between hyper-parameters for simplicity. The equations outlined above, combined with MCMC methods can be used to infer these $8\vec{\theta}'$ parameters from which the hierarchical population distribution can be determined.

In order to test whether this assumption of a multi-component Gaussian mixture model is appropriate, I sampled the inferred hierarchical distributions to produce replica datasets in optical-NUV colour space. These are shown here in Figure 2.7 in comparison to the observed colour-colour distributions of the INACTIVE sample (a subset of $\sim 6,000$ galaxies from the GZ2-GALEX sample, see Section 4.1). For all masses and morphologies the replicated $u - r$ and $NUV - u$ colours do not accurately match the observed data.

I also varied the value of N_s and found that increasing the number of samples drawn did not improve this fit for the INACTIVE population. Similarly increasing the number of components in the Gaussian mixture model did not immediately improve the accuracy of the fit. I therefore concluded that this functional form of the population distribution was unsatisfactory.

The POPSTARPY approach described in section 2.5 was motivated by the investigation increasing the number of samples, N_s drawn from the posterior of each galaxy, k , until the point where all the samples were drawn. Instead of attempting to infer parameters to describe this distribution, as above, I presented the distribution itself (as described in Section 2.5). The distributions produced by this visualisation method reveal the complexity that the parent distribution must describe which, as concluded earlier, cannot be effectively modelled.

I also tested whether the POPSTARPY method is reasonable by producing replica datasets in optical-NUV colour space, as before, by drawing 1000 $[t, \tau]$ values from the population density distributions derived for the INACTIVE sample (see Section 4.1). These replica datasets are shown here in Figure 2.8 in comparison to the observed colour-colour distributions of the INACTIVE sample. Comparing these replica colours in Figure 2.8, with those produced by drawing from the inferred hierarchical distributions, shown in Figure 2.7, they can be seen to produce a more accurate match to the observed data for the majority of masses and morphologies.

Considering these issues with assuming a functional form for the hierarchical parent distribution, an expansion on this approach would be to perform ‘heat map optimization’, similar to image reconstruction, to determine the parent distribution for a given population. Each pixel would need a prior (e.g. a basic entropic prior) and the heat map would sum to unity. This is a significant expansion upon the work presented here and is something the author wishes to investigate in future work.

For the results presented in the following chapters, I therefore use the POPSTARPY method to visualise the population distribution, rather than quoting inferred values to describe it.

Chapter 3

The morphological dependance of quenching

The work in the following chapter has been published in Smethurst et al. (2015).

Figure 3.1 shows the SFR versus the stellar mass for the observed GZ2 sample which has been split into blue cloud, green valley and red sequence populations as well as into the ‘clean’ disc and smooth galaxy samples (with GZ2 vote fractions of $p_d \geq 0.8$ and $p_s \geq 0.8$ respectively). The green valley galaxies are indeed a population which have either left, or begun to leave, the star forming sequence or have some residual star formation still occurring.

The left panel in Figure 2.1 shows a handful of quenching models and how they reproduce the observed relationship between the SFR and the mass of a galaxy, including how at the time of quenching they reside on the star forming sequence shown by the solid black line for a galaxy of mass, $M = 10^{10.27} M_\odot$. The right panel shows how these SFRs translate into the optical-NUV colour-colour plane to reproduce observed colours of green valley and red sequence galaxies. Some of the SFHs produce colours redder than the apparent peak of the red sequence in the GZ2 subsample; however this is not the *true* peak of the red sequence due to the necessity for NUV colours from GALEX (see Section 1.1).

The majority of the red galaxies in the sample therefore lie towards the *blue end* of the red sequence and have a small amount of residual star formation in order to be detected in the NUV resulting in a specific subset of the red sequence studied in this

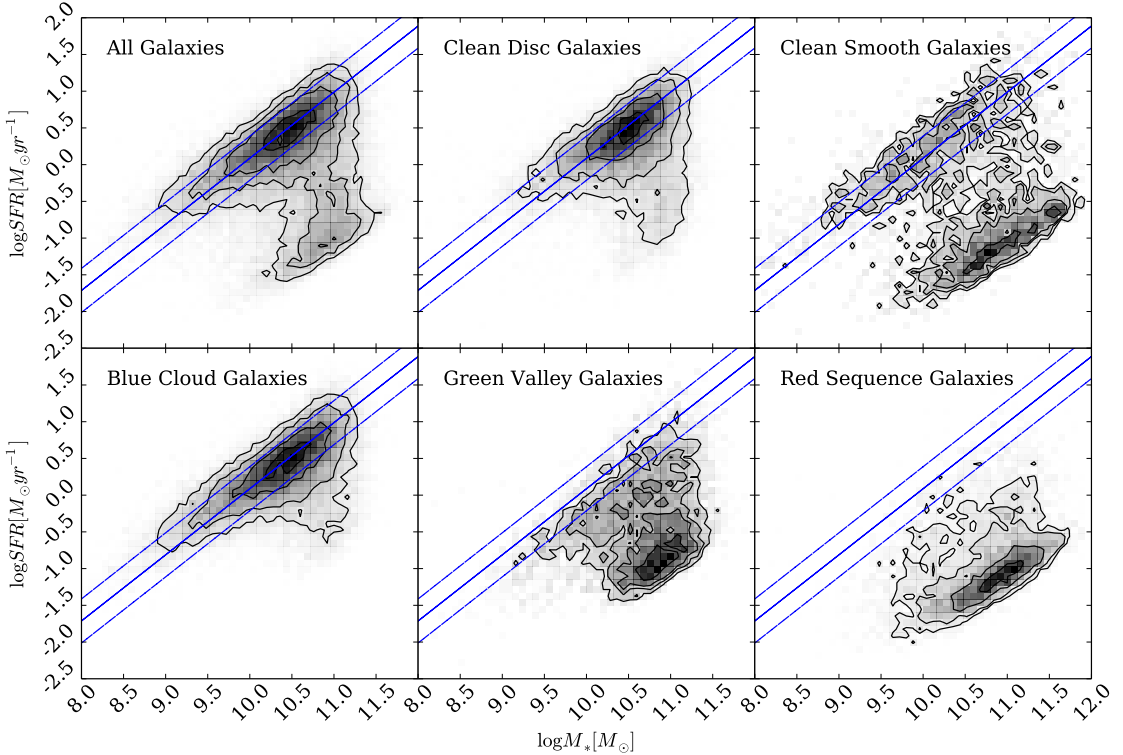


Figure 3.1: Star formation rate versus stellar mass diagrams show the different populations of galaxies (top row, left to right: all galaxies, GZ2 ‘clean’ disc and smooth galaxies; bottom row, left to right: blue cloud, green valley and red sequence galaxies) and how they contribute to the star forming sequence (from Peng et al. (2010), shown by the solid blue line with 0.3 dex scatter by the dashed lines). Based on positions in these diagrams, the green valley does appear to be a transitional population between the blue cloud and the red sequence. Detailed analysis of star formation histories can elucidate the nature of the different populations’ pathways through the green valley. The clean smooth and disc samples are described in Section 1.1.

investigation. Only 47% of the red sequence galaxies present in the entire Galaxy Zoo 2 sample are matched with GALEX to produce our final sample of 126,316 galaxies, as opposed to 72% of the blue cloud and 53% of the green valley galaxies. This limitation should be taken into account when considering the results in the following sections.

The SFH models were implemented with the STARPY package to produce Figures 3.2, 3.3 & 3.4 for the red sequence, green valley and blue cloud populations of smooth and disc galaxies respectively. The percentages shown in Figures 3.2, 3.3 & 3.4 are calculated as the fractions of the combined posterior probability distribution located in each region of parameter space for a given population.

Since the sample contains such a large number of galaxies, we interpret these fractions as broadly equivalent to the percentage of galaxies in a given population undergoing quenching within the stated timescale range. Although this is not quantitatively exact, it is nevertheless a useful framework for interpreting the results of combining the individual posterior probability distributions of each galaxy.

Also shown in Figure 11 are the median walker positions (the 50th percentile of the Bayesian probability distribution) of each individual galaxy, split into red, green and blue populations also with a hard cut in the vote fraction of $p_d > 0.5$ and $p_s > 0.5$ to show the disc and smooth populations respectively. These positions were calculated without discarding any walker positions due to low probability and without weighting by vote fractions; therefore this may be more intuitive to understand than Figures 3.2, 3.3 & 3.4.

Although the quenching timescales are continuous in nature, in this Section we refer to rapid, intermediate and slow quenching timescales which correspond to ranges of τ [Gyr] < 1.0 , $1.0 < \tau$ [Gyr] < 2.0 and τ [Gyr] > 2.0 respectively for ease of discussion.

3.1 The Red Sample

The left panel of Figure 3.2 reveals that smooth galaxies with red optical colours show a preference (49.5%; see Figure 3.2) for rapid quenching timescales across all cosmic time resulting in a very low current SFR. For these smooth red galaxies we

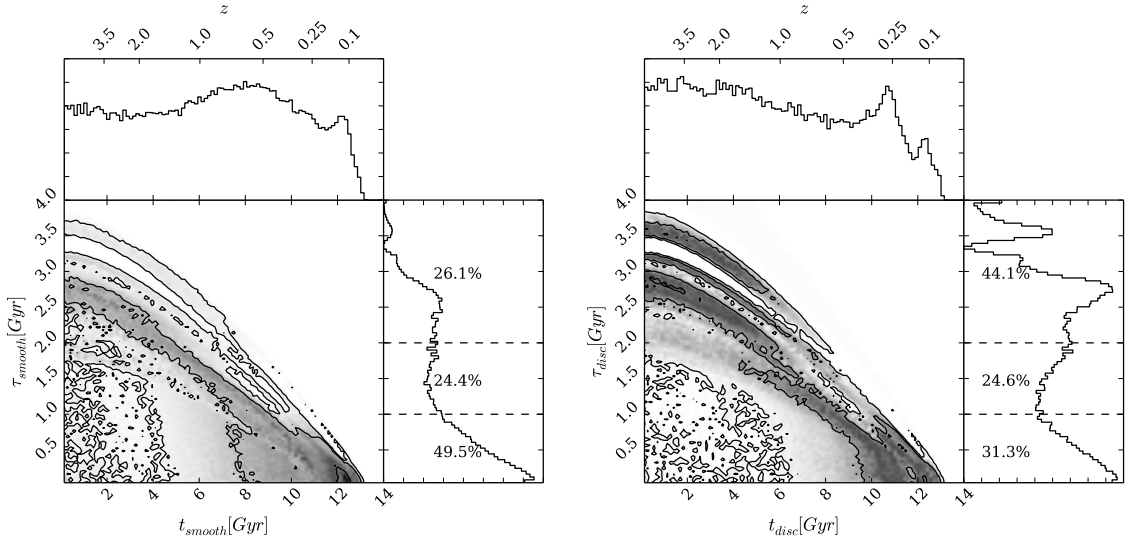


Figure 3.2: Contour plots showing the combined positions in the Markov Chain for all red galaxies in this study, weighted by the logarithmic probability of each position (see Section 2.2) and also by the morphological vote fractions from GZ2 to give the areas of high probability in the model parameter space for both bulge (left) and disc (right) dominated systems. The histograms show the projection into one dimension for each parameter. The dashed lines show the separation between rapid ($\tau [\text{Gyr}] < 1.0$), intermediate ($1.0 < \tau [\text{Gyr}] < 2.0$) and slow ($\tau [\text{Gyr}] > 2.0$) quenching timescales with the fraction of the combined posterior probability distribution in each region shown (see Section 2.2).

see, at early times only, a preference for slow and intermediate timescales in the left panel of Figure 3.2. Perhaps this is the influence of intermediate galaxies (with $p_s \sim p_d \sim 0.5$), hence why similar high probability areas exist for both the smooth-like and disc-like galaxies in the left and right panels of Figure 3.2. This is especially apparent considering there are far more of these intermediate galaxies than those that are definitively early- or late-types (see Table ??). These galaxies are those whose morphology cannot be easily distinguished either because they are at a large distance or because they are an S0 galaxy whose morphology can be interpreted by different users in different ways. Willett et al. (2013) find that S0 galaxies expertly classified by Nair & Abraham (2010) are more commonly classified as ellipticals by GZ2 users, but have a significant tail to high disc vote fractions, giving a possible explanation as to the origin of this area of probability.

The right panel of Figure 3.2 reveals that red disc galaxies show similar preferences for rapid (31.3%) and slow (44.1%) quenching timescales. The preference for *very* slow ($\tau > 3.0$ Gyr) quenching timescales (which are not seen in either the green valley or blue cloud, see Figures 3.3 and 3.4) suggests that these galaxies have only just reached the red sequence after a very slow evolution across the colour-magnitude diagram. Considering their limited number and our requirement for NUV emission, it is likely that these galaxies are currently on the edge of the red sequence having recently (and finally) moved out of the green valley. Table ?? shows that 3.9% of our sample are red sequence clean disc galaxies, i.e. red late-type spirals. This is, within uncertainties, in agreement with the findings of Masters et al. (2010a), who find $\sim 6\%$ of late-type spirals are red when defined by a cut in the $g - r$ optical colour (rather than with $u - r$ as implemented in this investigation) and are at the ‘blue end of the red sequence’.

Despite the dominance of slow quenching timescales, the red disc galaxies also show some preference for rapid quenching timescales (31.3%), similar to the red smooth galaxies but with a lower probability. Perhaps these rapid quenching timescales can also be attributed to a morphological change, suggesting that the quenching has occurred more rapidly than the morphological change to a bulge dominated system.

Comparing the resultant SFRs for both the smooth- and disc-like galaxies in Figure 3.2 by noticing where the areas of high probability lie with respect to the bottom panel of Figure 2.2 (which shows the predicted SFR at an observation time of $t \sim 12.8$ Gyr, the average ‘observed’ time of the GZ2 population) reveals that

red disc galaxies with a preference for slow quenching still have some residual star formation occurring, $\text{SFR} \sim 0.105 M_{\odot} \text{yr}^{-1}$, whereas the smooth galaxies with a dominant preference for rapid quenching have a resultant $\text{SFR} \sim 0.0075 M_{\odot} \text{yr}^{-1}$. This is approximately 14 times less than the residual SFR still occurring in the red sequence disc galaxies. Within error, this is in agreement with the findings of Tojeiro et al. (2013) who, by using the VErsatile SPectral Analyses spectral fitting code (VESPA; Tojeiro et al. 2007), found that red late-type spirals show 17 times more recent star formation than red elliptical galaxies.

These results for the red galaxies investigated here with NUV emission, have many implications for green valley galaxies, as all of these systems must have passed through the green valley on their way to the red sequence.

3.2 Green Valley Galaxies

In Figure 3.3 we can make similar comparisons for the green valley galaxies to those discussed previously for the subset of red galaxies studied. For the red galaxies, an argument can be made for two possible tracks across the green valley, shown by the bimodal nature of both distributions in τ with a common area in the intermediate timescales region where the rapid and slow timescales peaked distributions intersect. However in the green valley this intermediate quenching timescale region becomes more significant (in agreement with the conclusions of Gonçalves et al. 2012), particularly for the smooth-like galaxies (see the left panel of Figure 3.3).

The smooth galaxy parameters favour these intermediate quenching timescales (40.6%) with some preference for slow quenching at early times ($z > 1$). The preference for rapid quenching of smooth galaxies has dropped by over a half compared to the red galaxies, however this will be influenced by the observability of galaxies undergoing such a rapid quench which will spend significantly less time in the transitional population of the green valley. Those galaxies with such a rapid decline in star formation will pass so quickly through the green valley they will be detected at a lower number than those galaxies which have stalled in the green valley with intermediate quenching timescales; accounting for the observed number of intermediate galaxies which are present in the green valley and the dominance of rapid timescales detected for red galaxies for both morphologies.

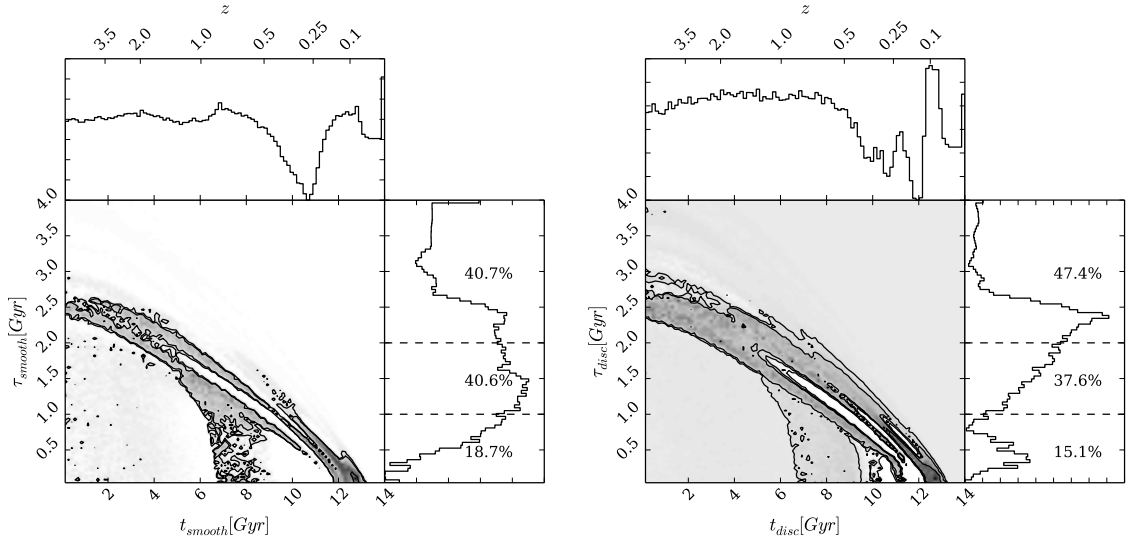


Figure 3.3: Contour plots showing the combined positions in the Markov Chain for galaxies in the green valley, weighted by the logarithmic probability of each position (see Section 2.2) and also by the morphological vote fractions from GZ2 to give the areas of high probability in the model parameter space for both bulge (left) and disc (right) dominated systems. The histograms show the projection into one dimension for each parameter. The dashed lines show the separation between rapid (τ [Gyr] $<$ 1.0), intermediate (1.0 $<$ τ [Gyr] $<$ 2.0) and slow (τ [Gyr] $>$ 2.0) quenching timescales with the fraction of the combined posterior probability distribution in each region shown (see Section 2.2).

The disc galaxies of the green valley now overwhelmingly prefer slow quenching timescales (47.4%) with a similar amount of intermediate quenching compared to the smooth galaxy parameters (37.6%; see Figure 3.3). There is still some preference for galaxies with a star formation history which results in a high current SFR, suggesting there are also some late-type galaxies that have just progressed from the blue cloud into the green valley.

If we compare Figure 3.3 to Figure 3.2 we can see quenching has occurred at later (more recent) cosmic times in the green valley at least for red galaxies for both morphological types. Therefore both morphologies are tracing the evolution of the red sequence, confirming that the green valley is indeed a transitional population between blue cloud and red sequence regardless of morphology. Currently as we observe the green valley, its main constituents are very slowly evolving disc-like galaxies along with intermediate- and smooth-like galaxies which pass across it with intermediate timescales within $\sim 1.0 - 1.5$ Gyr.

Given enough time ($t \sim 4 - 5$ Gyr), the disc galaxies will eventually fully pass through the green valley and make it out to the red sequence (the right panel of Figure 2.1 shows galaxies with $\tau > 1.0$ Gyr do not approach the red sequence within 3 Gyr post quench). This is most likely the origin of the ‘red spirals’.

If we consider then that the green valley is a transitional population, then we can expect that the ratio of smooth:disc galaxies that is currently observed in the green valley will evolve into the ratio observed for the red galaxies with NUV emission investigated. Table ?? shows the ratio of smooth : disc galaxies in the observed red sequence of the GZ2 sample is 62 : 38 whereas in the green valley it is 45 : 55. Making the very simple assumptions that this ratio does not change with redshift and that quenching is the only mechanism which causes a morphological transformation, we can infer that 31.2% of the disc-dominated galaxies currently residing in the green valley would have to undergo a morphological change to a bulge-dominated galaxy. We find that the fraction of the probability for green valley disc galaxies occupying the parameter space $\tau < 1.5$ Gyr is 29.4%, and therefore suggest that quenching mechanisms with these timescales are capable of destroying the disc-dominated nature of galaxies. This is most likely an overestimate of the mechanisms with timescales that can cause a morphological change because of the observability of those galaxies which undergo such a rapid quench; Martin et al. (2007) showed that after considering

the time spent in the green valley, the fraction of galaxies undergoing a rapid quench quadruples.

All of this evidence suggests that there are not just two routes for galaxies through the green valley as concluded by S14, but a continuum of quenching timescales which we can divide into three general regimes: rapid ($\tau < 1.0$ Gyr), intermediate ($1.0 < \tau < 2.0$ Gyr) and slow ($\tau > 2.0$ Gyr). The intermediate quenching timescales reside in the space between the extremes sampled by the UV/optical diagrams of S14; the inclusion of the intermediate galaxies in this investigation (unlike in S14) and the more precise Bayesian analysis, quantifies this range of τ and specifically ties the intermediate timescales to all variations of galaxy morphology.

3.3 Blue Cloud Galaxies

Since the blue cloud is considered to be primarily made of star forming galaxies we expect STARPY to have some difficulty in determining the most likely quenching model to describe them, as confirmed by Figure 3.4. The attempt to characterise a star forming galaxy with a quenched SFH model leads STARPY to attribute the extremely blue colours of the majority of these galaxies to fast quenching at recent times (i.e. very little change in the SFR; see the right panel of Figure 3.4 in comparison with the bottom panel of Figure 2.2).

This is particularly apparent for the blue disc population. Perhaps even galaxies which are currently quenching slowly across the blue cloud cannot be well fit by the quenching models implemented, as they still have high SFRs despite some quenching (although a galaxy has undergone quenching, star formation can still occur in a galaxy, just at a slower rate than at earlier times, described by τ).

There is a very small preference among blue bulge dominated galaxies for slow quenching which began prior to $z \sim 0.5$. These populations have been blue for a considerable period of time, slowly using up their gas for star formation by the Kennicutt–Schmidt law (Schmidt, 1959; Kennicutt, 1997). However the major preference is for rapid quenching at recent times in the blue cloud; this therefore provides some support to the theories for blue ellipticals as either merger-driven ($\sim 76\%$; like those identified as recently quenched ellipticals with properties consistent with a

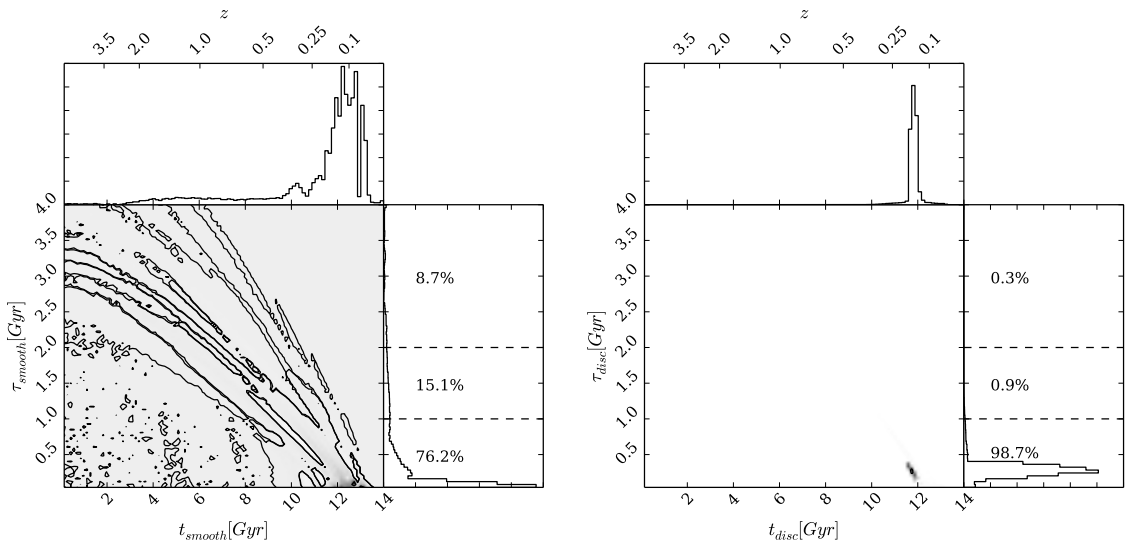


Figure 3.4: Contour plots showing the combined positions in the Markov Chain for galaxies in the blue cloud, weighted by the logarithmic probability of each position (see Section 2.2) and also by the morphological vote fractions from GZ2 to give the areas of high probability in the model parameter space for both bulge (left) and disc (right) dominated systems. The histograms show the projection into one dimension for each parameter. The dashed lines show the separation between rapid (τ [Gyr] < 1.0), intermediate ($1.0 < \tau$ [Gyr] < 2.0) and slow (τ [Gyr] > 2.0) quenching timescales with the fraction of the combined posterior probability distribution in each region shown (see Section 2.2). Positions with probabilities less than 0.2 are discarded as poorly fit models, therefore we can conclude unsurprisingly that blue cloud galaxies are not well described by a quenching star formation model.

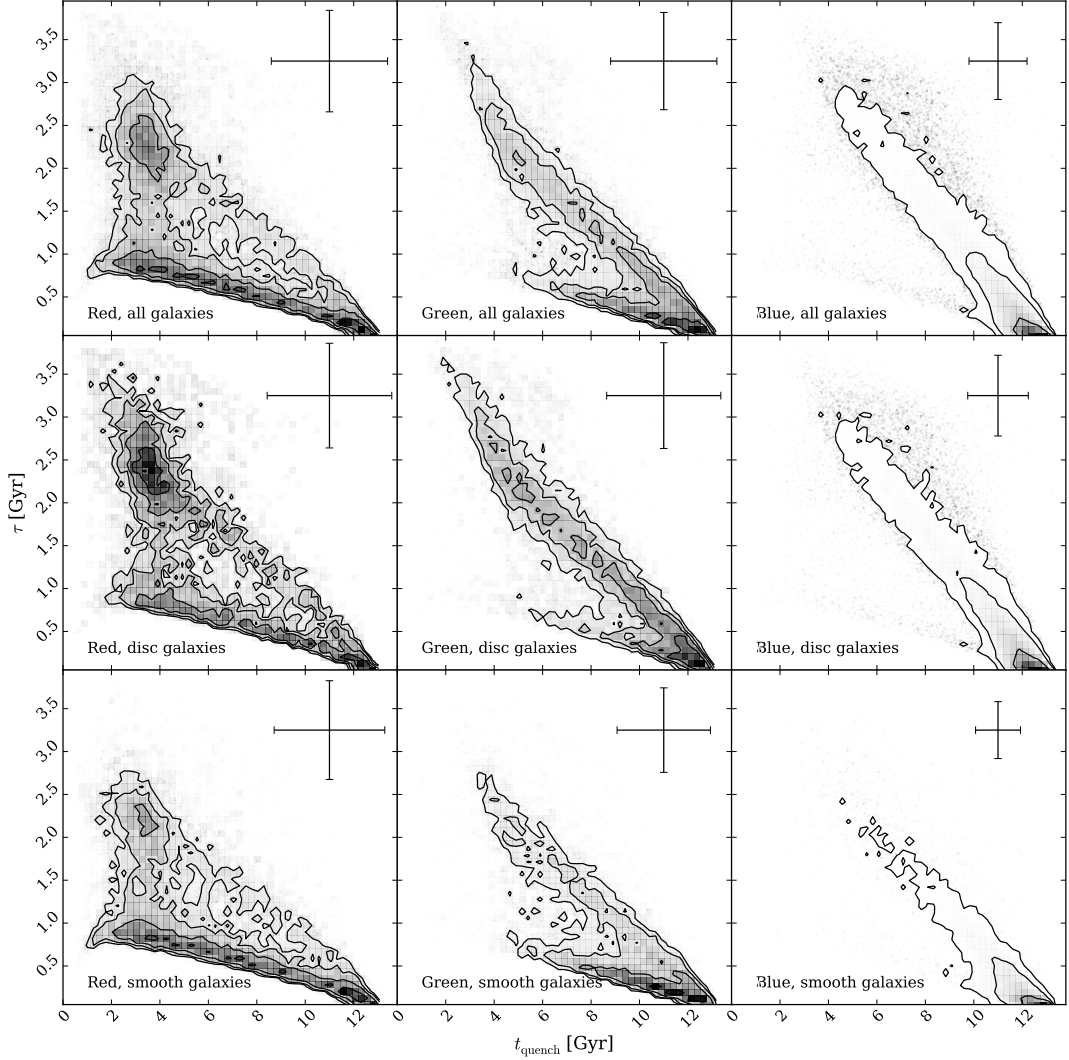


Figure 3.5: Contours showing the positions in the $[t, \tau]$ parameter space of the median walker position (the 50th percentile; as shown by the intersection of the solid blue lines in Figure 2.2) for each galaxy for all (top), disc ($p_d > 0.5$; middle), and smooth ($p_s > 0.5$; bottom) red sequence, green valley and blue cloud galaxies in the left, middle and right panels respectively. The error bars on each panel shows the average 68% confidence on the median positions (calculated from the 16th and 84th percentile, as shown by the blue dashed lines in Figure 2.2). These positions were calculated without discarding any walker positions due to low probability and without weighting by vote fractions, therefore this plot may be more intuitive than Figures 3.2, 3.3 & 3.4. The differences between the smooth and disc populations and between the red, green and blue populations remain clearly apparent.

merger origin by McIntosh et al. 2014) or gas inflow-driven reinvigorated star formation that is now slowly decreasing ($\sim 24\%$; such as the population of blue spheroidal galaxies studied by Kaviraj et al. 2013). However, we remind the reader that the quenching models used in this work do not provide an adequate fit to the blue cloud population.

The blue cloud is therefore primarily composed of both star forming galaxies with any morphology and smooth galaxies which are undergoing a rapid quench, presumably after a previous event triggered star formation and turned them blue.

3.3.1 Discussion

Chapter 4

Black hole-galaxy co-evolution in the context of quenching

The work in the following chapter has been published in Smethurst et al. (2016).

4.1 Rapid, recent quenching within a population of Type 2 AGN host galaxies

4.1.1 AGN Sample

We selected Type 2 AGN from the GZ2-GALEX sample using a BPT diagram (Baldwin et al., 1981) using line and continuum strengths for [OIII], [NII], [SII] and [OII] obtained from the MPA-JHU catalogue (Kauffmann et al., 2003b; Brinchmann et al.,

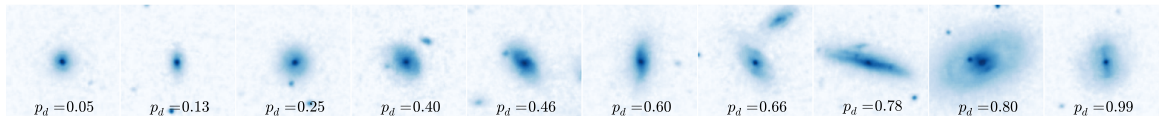


Figure 4.1: Randomly selected SDSS *gri* composite images from the sample of 1,244 Type 2 AGN in a redshift range $0.04 < z < 0.05$. The galaxies are ordered from least to most featured according to their debiased ‘disc or featured’ vote fraction, p_d (see Willett et al. 2013). The scale for each image is 0.099 arcsec/pixel.

2004). We then required the $S/N > 3$ for each emission line as in Schawinski et al. (2010). Those galaxies which satisfied all of the inequalities defined in Kewley et al. (2001) and Kauffmann et al. (2003a) were selected as Type 2 AGN, giving 1,299 host galaxies ($\sim 10\%$ of the GZ2-GALEX sample). Sarzi et al. (2010); Yan & Blanton (2012) and Singh et al. (2013) have all demonstrated that LINERs are not primarily powered by AGN, therefore for purity, we excluded these galaxies from the sample using the definition from Kewley et al. (2006) (55 galaxies total) with no change to the results. These 1,244 galaxies will be referred to as the AGN-HOST sample.

We refrain from using Type 1 AGN due to concerns about contamination of the SFH analysis from potentially strong NUV emission by unobscured nuclei. The obscuration of Type 2 AGN is highly efficient, considerably more so in the NUV than the optical (Simmons et al., 2011); residual NUV flux from a Type 2 AGN can be neglected in comparison to that of the galaxy. We also investigated the possibility of contamination of optical galaxy colours by residual AGN emission, finding that subtracting measured nuclear magnitudes (SDSS `psfMag`) produces a negligible change in host galaxy colour ($\Delta(u - r) \sim 0.09$). We therefore use the uncorrected colours to avoid unnecessary complexity and minimise the propagation of uncertainty from the colours through to the SFHs. However, we note that including these corrected colours does not change our results.

We note also that galaxy colours were not corrected for intrinsic dust attenuation. This is of particular consequence for disc galaxies, where attenuation increases with increasing inclination. Buat et al. (2005) found the median value of the attenuation in the GALEX NUV passband to be ~ 1 mag. Similarly Masters et al. (2010b) found a total extinction from face-on to edge-on spirals of 0.7 and 0.5 mag for the SDSS u and r passbands and show spirals with $\log(a/b) > 0.7$ have signs of significant dust attenuation. For the AGN-HOST (INACTIVE) sample we find 23% (25%) of discs (with $p_d > 0.5$) have $\log(a/b) > 0.7$, therefore we must be aware of possible biases in our results due to dust.

From the findings of Masters et al. (2010b) and Buat et al. (2005) above, we estimate the extinction to be $u - r \sim 0.2$ mag and $NUV - u \sim 0.3$ mag, therefore the average change in the SFH parameters across a range of input colours $0 < u - r < 4$ and $-1 < NUV - u < 5$, are $\Delta t_q = 0.985$ Gyr, $\Delta \tau = 1.571$ Gyr. This change therefore causes the SFH parameters derived to move towards earlier times and faster quenching rates. Results should be viewed with the caveat, particularly for higher

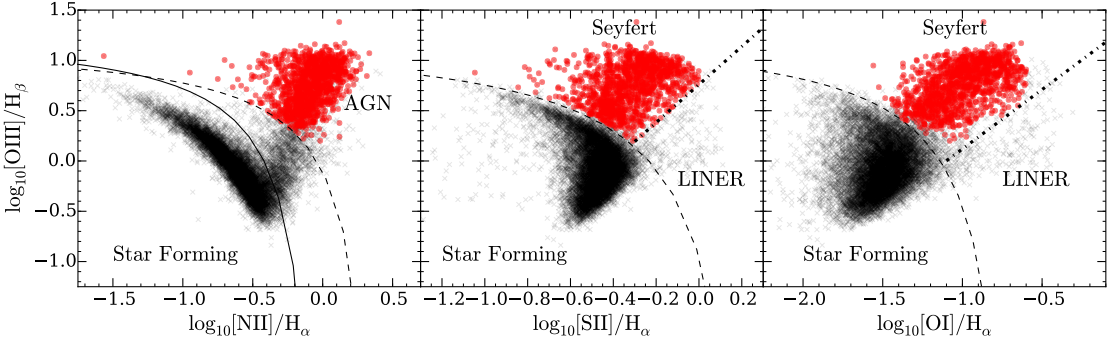


Figure 4.2: BPT diagrams for galaxies in the GZ2-GALEX sample (black crosses) with $S/N > 3$ for each emission line. Inequalities defined in: Kewley et al. (2001) to separate SF galaxies from AGN (dashed lines), Kauffmann et al. (2003a) to separate SF from composite SF-AGN galaxies (solid line) and Kewley et al. (2006) to separate LINERS and Seyferts (dotted lines). Galaxies are included in the AGN-HOST sample (red circles) if they satisfy all the inequalities to be classified as Seyferts. LINERS are excluded for purity.

mass, disc galaxies, that earlier values of t_q and more rapid values of τ may be inferred by STARPY. However, we note that (i) applying these average corrections across each sample population does not change our main conclusions, (ii) that results are consistent if the population of edge-on and face-on galaxies are compared and (iii) that results do not change if only face-on galaxies are used in the investigation, strongly suggesting that internal galactic extinction does not systematically bias our results.

SDSS images for 10 randomly selected galaxies from the AGN-HOST sample are shown in Figure 4.1; Figure 4.2 shows the entire AGN-HOST sample and the matched GZ2-GALEX galaxies on a BPT diagram. For the AGN-HOST sample the mean $\log(L[OIII][\text{erg s}^{-1}]) = 41.3$ and median $\log(L[OIII][\text{erg s}^{-1}]) \sim 41.0$, with a range of $\log(L[OIII][\text{erg s}^{-1}])$ luminosities of $39.4 - 43.0$.

We constructed a control sample of inactive galaxies by removing from the GZ2-GALEX sample all galaxies with line strengths indicative of potential AGN activity (Kauffmann, Heckman, Tremonti, Brinchmann, Charlot, White, Ridgway, Brinkmann, Fukugita, Hall, Ivezić, Richards, & Schneider, 2003a), as well as sources identified as Type 1 AGN by the presence of broad emission lines (Oh et al., 2015). We select mass- and morphology-matched inactive samples by identifying between 1 and 5 inactive

galaxies for each AGN-HOST galaxy with the same stellar mass (to within $\pm 5\%$) and GZ2 ‘smooth’ and ‘disc’ vote fractions (to within ± 0.1); this selects 6107 galaxies. We refer to this sample as the INACTIVE sample. A Kolmogorov-Smirnov test revealed the redshift distributions of the INACTIVE and AGN-HOST samples are statistically indistinguishable ($D \sim 0.16$, $p \sim 0.88$).

We show the AGN-HOST and INACTIVE samples on both an optical colour-magnitude diagram and in the SFR-stellar mass plane in Figure 4.3 in comparison to the distribution of SDSS DR7 galaxies. SFRs and stellar masses are obtained from the MPA JHU catalog, where available, which follow the prescriptions outlined in Brinchmann et al. (2004) and Salim et al. (2007) for calculating the total aperture corrected galaxy SFR in the presence of an AGN.

We note that the majority of the AGN-HOST sample would be defined as residing in the blue cloud (73%) on the optical colour-magnitude diagram despite the fact that a significant proportion of the sample (47%) lie more than 1σ (0.3 dex) below the star forming “main sequence” (fit to the MPA-JHU catalog of SDSS DR7 of Kauffmann et al. 2003b; Brinchmann et al. 2004, see Figure 4.3).

Ko et al. (2013) show that in a sample of quiescent red-sequence galaxies without H α emission, 26% show NUV excess emission and that the fraction with recent star formation is 39%. This is more clearly visible in Figure 4.3b, where a substantial fraction of both the AGN-HOST and INACTIVE samples, all of the sources in which have detected NUV emission, nevertheless lie more than 1σ below the star-formation sequence. We do not make a cut on either the AGN-HOST or INACTIVE samples for star formation rate. The SFH of the entire samples are fitted, however we describe in Section ?? how our method accounts for those galaxies not appropriately fit by a quenching model and down-weights their contribution to the final results.

Since this investigation is focussed on whether an AGN can have an impact on the SF of its host galaxy, we must also consider possible selection effects. The extent to which SF could obscure AGN emission was addressed by Schawinski et al. (2010). They showed, via analysis of simulated AGN emission added to star-forming galaxies, that BPT-based selection of AGN produces a complete sample at luminosities of $L[OIII] > 10^{40}$ erg s $^{-1}$. Above this limit we therefore assume we have selected a complete sample of AGN independent of host galaxy SFR.

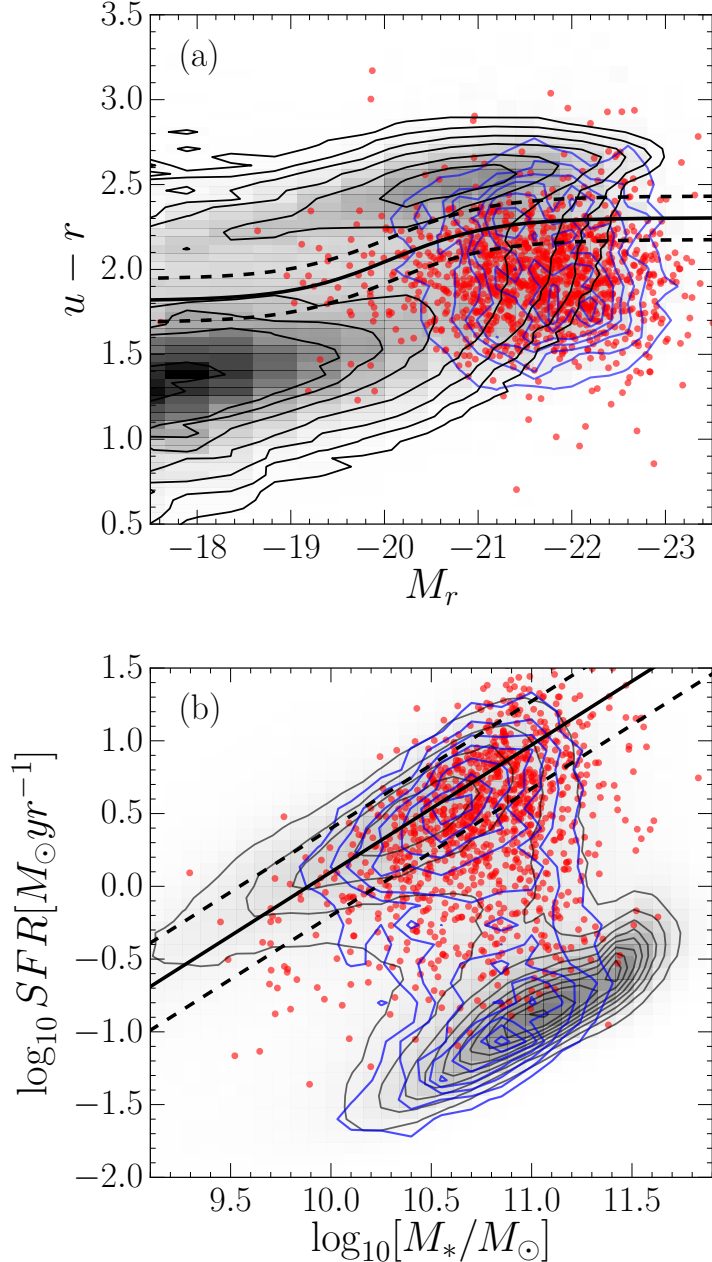


Figure 4.3: (a) Optical colour-magnitude diagram showing the SDSS DR7 (grey filled contours), the AGN-HOST sample (red circles) and INACTIVE sample (blue contours). The definition of the green valley from Baldry et al. (2006) (solid line) with $\pm 1\sigma$ (dashed lines) is shown. (b) SFR-stellar mass diagram showing the MPA-JHU measurements of SFR and M_* of SDSS DR7 galaxies (Kauffmann et al. 2003b; Brinchmann et al. 2004; black contours), the AGN-HOST sample (red circles) and INACTIVE sample (blue contours). The star forming “main sequence” from Peng et al. (2010) is shown by the solid line for $t = 12.8$ Gyr, the average observed age of the GZ2-GALEX sample, with $\pm 1\sigma$ (dashed lines).

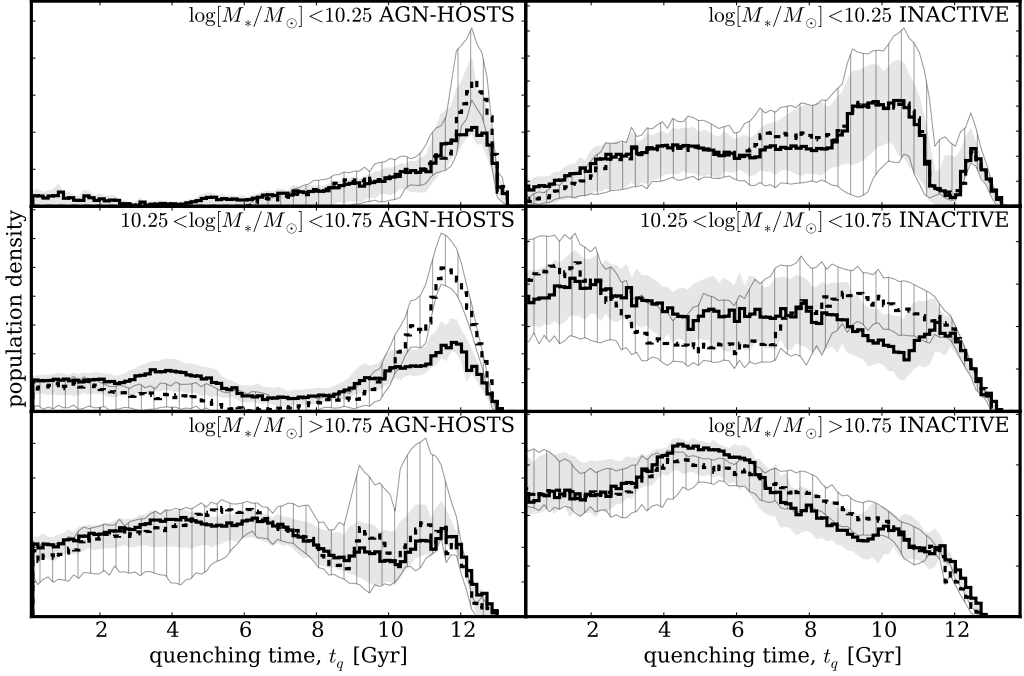


Figure 4.4: Population density distributions for the quenching time (t_q) parameter, normalised so that the areas under the curves are equal. AGN-HOST (left) and INACTIVE (right) galaxies are split into low (top), medium (middle) and high (bottom) mass for smooth (dashed) and disc (solid) galaxies. Uncertainties from bootstrapping are shown by the shaded regions for the smooth (grey striped) and disc (grey solid) population densities. A low (high) value of t_q corresponds to the early (recent) Universe.

4.1.2 Results

Figures 4.4 and 4.5 show the stacked population density distributions for the quenching time, t_q and exponential quenching rate, τ , respectively. In each figure the population density, along with shaded regions to show the uncertainties, for a given parameter is shown for smooth and disc galaxy populations across three mass bins for the AGN-HOST and INACTIVE samples. No cut on the star formation rate is made to the galaxies which contribute to Figures 4.4 & 4.5, but those galaxies poorly fit by an exponentially declining SFH are down-weighted so that they do not contribute to the results presented here. In Table 4.1 the percentage of the population density in each quenching regime for rapid ($\tau < 1$ Gyr), intermediate ($1 < \tau$ [Gyr] < 2) and slow ($\tau > 2$ Gyr) quenching timescales, are shown. Uncertainties on the popula-

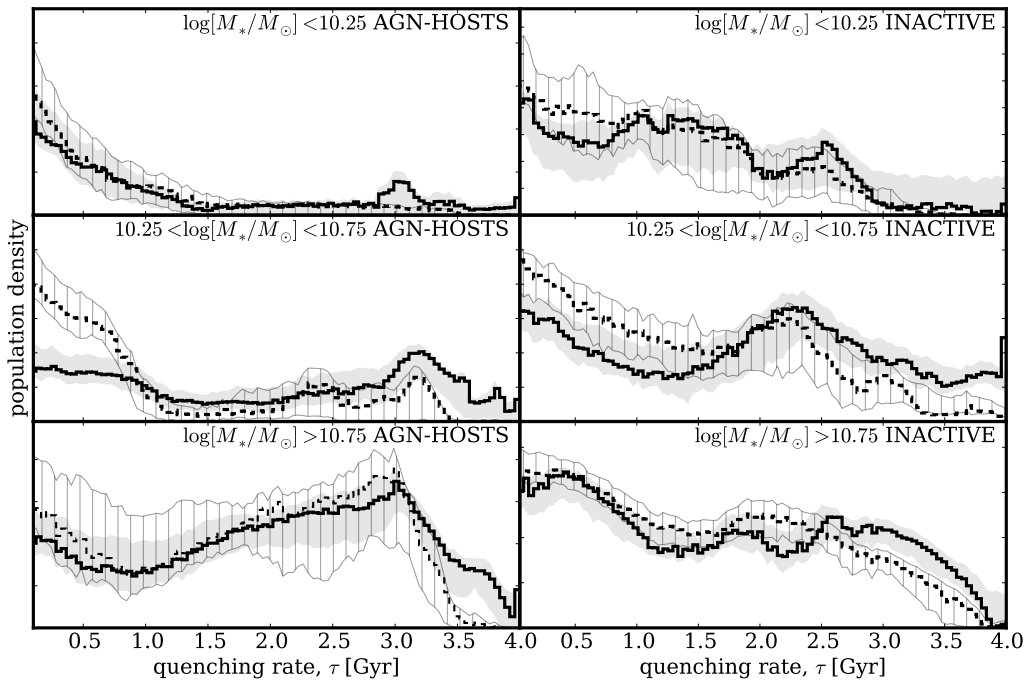


Figure 4.5: Population density distributions for the quenching rate (τ), normalised so that the areas under the curves are equal. AGN-HOST (left) host and INACTIVE (right) galaxies are split into low (top), medium (middle) and high (bottom) mass for smooth (dashed) and disc (solid) galaxies. Uncertainties from bootstrapping are shown by the shaded regions for the smooth (grey striped) and disc (grey solid) population densities. A small (large) value of τ corresponds to a rapid (slow) quench.

Table 4.1: Table showing the number of galaxies in each of the three mass bins for both the AGN-HOSTS and INACTIVE galaxy samples and the percentage of the distribution across each morphologically weighted population found in the rapid, intermediate and slow quenching regimes.

SAMPLE	MASS BIN	WEIGHTING	$\tau < 1$ [Gyr]	$1 < \tau$ [Gyr] < 2	$\tau > 2$
AGN-HOSTS	$\log[M_*/M_\odot] < 10.25$	p_d	$60 \pm^{23}_5$	$13 \pm^9_9$	$2 \pm^2_2$
		p_s	$69 \pm^{14}_6$	$17 \pm^6_{14}$	
	$10.25 < \log[M_*/M_\odot] < 10.75$	p_d	$33 \pm^3_5$	$15 \pm^4_4$	
		p_s	$69 \pm^4_5$	$7 \pm^4_4$	
	$\log[M_*/M_\odot] > 10.75$	p_d	$20 \pm^5_4$	$25 \pm^7_5$	$5 \pm^5_5$
		p_s	$24 \pm^4_3$	$26 \pm^5_6$	
INACTIVE	$\log[M_*/M_\odot] < 10.25$	p_d	$37 \pm^8_{14}$	$39 \pm^8_6$	$1 \pm^1_1$
		p_s	$47 \pm^5_{11}$	$36 \pm^9_5$	
	$10.25 < \log[M_*/M_\odot] < 10.75$	p_d	$30 \pm^4_3$	$18 \pm^2_3$	
		p_s	$42 \pm^2_2$	$29 \pm^3_3$	
	$\log[M_*/M_\odot] > 10.75$	p_d	$36 \pm^3_3$	$24 \pm^3_4$	
		p_s	$38 \pm^2_2$	$28 \pm^3_4$	

tion densities (shown by the shaded regions) are determined from the maximum and minimum values spanned by $N = 1000$ bootstrap iterations, each sampling 90% of the galaxy population. 1σ uncertainties are quoted for the percentages in Table 4.1, calculated from the bootstrapped distributions.

These population densities should be interpreted as the spread of quenching times and rates occurring in galaxies which have either undergone or are undergoing quenching within a population. Figures 4.4 and 4.5 show a distinct difference between the population density of AGN-HOST and INACTIVE quenching parameters.

At all masses, the population density for galaxies within the AGN-HOST population across the quenching time t_q parameter (left panels of Figure 4.4) is different from that of the inactive galaxies (right panels of Figure 4.4). Recent quenching ($t > 11$ Gyr) is the dominant history for quenched and quenching low and medium mass AGN-HOST galaxies, particularly for the smooth galaxies hosting an AGN. However, this effect is less dominant in higher mass galaxies where quenching at earlier times also has high density.

The population densities for the quenching rate, τ , in Figure 4.5 and Table 4.1

show the dominance of rapid quenching ($\tau < 1$ Gyr) within the AGN-HOST population, particularly for smooth galaxies. With increasing mass the dominant quenching rate becomes slow ($\tau > 2$ Gyr) especially for disc galaxies hosting an AGN. Similar trends in the density are observed within the INACTIVE population but the overall distribution is very different.

The distributions for the AGN-HOST galaxies therefore show evidence for the dominance of rapid, recent quenching within this population. This result implies the importance of AGN feedback for the evolution of these galaxies.

4.1.3 Discussion

The differences between the population density distributions of the AGN-HOST and INACTIVE populations reveal that an AGN can have a significant effect on the SFH of its host galaxy. Both recent, rapid quenching and early, slow quenching are observed in the population density within the AGN-HOST population.

There are minimal differences between the smooth and disc weighted distributions of the quenching parameters within the AGN-HOST population. This is agreement with the conclusions of Kauffmann et al. (2003a) who found that the structural properties of AGN hosts depend very little on AGN power.

The difference between the AGN-HOST and INACTIVE population distributions in Figure 4.5 for the rate of quenching, τ , tells a story of gas reservoirs. The density distribution for higher mass AGN-HOST galaxies is dominated by slow, early quenching implying another mechanism is responsible for the cessation of star formation within a proportion of these high mass galaxies prior to the triggering of the current AGN. This preference for slow evolution timescales follows from the ideas of previously isolated discs evolving slowly by the Kennicutt-Schmidt (Schmidt, 1959; Kennicutt, 1997) law which can then undergo an interaction or merger to reinvigorate star formation, feed the central black hole and trigger an AGN (Varela et al., 2004; Emsellem et al., 2015). These galaxies would need a large enough gas reservoir to fuel both SF throughout their lifetimes and the recent AGN. These high mass galaxies also play host to the most luminous AGN (mean $\log(L[OIII] [\text{erg s}^{-1}]) \sim 41.6$) and so this SFH challenges the usual explanation for the co-evolution of luminous black holes and their host galaxies driven by merger growth.

Quenching at early times is also observed within a subsample of the INACTIVE population, where the density for the quenching time is roughly constant until recent times where the distribution drops off. This drop-off occurs at earlier times with increasing mass with a significant lack of quenching occurring at early times for low mass INACTIVE galaxies (right panels Figure 4.4). This is evidence of downsizing within the INACTIVE galaxy population whereby stars in massive galaxies form first and quench early (Cowie et al., 1996; Thomas et al., 2010).

Some of the most massive AGN-HOST galaxies also show a preference for earlier quenching (bottom left panel Figure 4.4) occurring at slow rates; we speculate that this is also due to the effects of downsizing rather than being caused by the current AGN. This earlier evolution would first form a slowly ‘dying’ or ‘dead’ galaxy typical of massive elliptical galaxies which can then have a recent infall of gas either through a minor merger, galaxy interaction or environmental change, triggering further star formation and feeding the central black hole, triggering an AGN (Kaviraj, 2014). In turn this AGN can then quench the recent boost in star formation. This track is similar to the evolution history proposed for blue ellipticals (Kaviraj et al., 2013; McIntosh et al., 2014; Haines et al., 2015). This SFH would then give rise to the distribution seen within the high mass AGN-HOST population for both time and rate parameters.

These recently triggered AGN in both massive disc and smooth galaxies do not have the ability to impact the SF across the entirety of a high mass galaxy in a deep gravitational potential (Ishibashi & Fabian, 2012; Zinn et al., 2013). This leads to the lower peak for recent, rapid quenching within the high mass AGN-HOST population for both morphologies.

Conversely, rapid quenching, possibly caused by the AGN itself through negative feedback, is the most dominant history within the low mass AGN-HOST population with lower gravitational potentials from which gas may be more readily expelled or heated (Tortora et al., 2009).

Tortora et al. (2009) model the effects of jet-induced AGN feedback on a typical early type (i.e. smooth) galaxy and observe a drastic suppression of star formation on a timescale of ~ 3 Myr. Comparing their synthetic colours with observed colours of SDSS elliptical galaxies, they find the time between the current galaxy age, t_{gal} and the time that the feedback began, t_{AGN} , peaks at $t_{\text{gal}} - t_{\text{AGN}} \sim 0.85$ Gyr. This

agrees with the location of the peak in Figure 4.4 for low mass galaxies which have undergone quenching, where the difference between the peak of the distribution and the average age of the population (galaxy age is calculated as the age of the Universe at the observed redshift, by assuming all galaxies form at $t = 0$) is ~ 0.83 Gyr. This implies that this SFH dominated by recent quenching is caused directly by negative AGN feedback.

However, there still remains the possibility that the AGN is merely a consequence of an alternative quenching mechanism. This idea is supported by simulations showing that the exhaustion of gas by a merger fuelled starburst could cause such a rapid quench in star formation and in turn also trigger an AGN (Croton et al., 2006; Wild et al., 2009; Snyder et al., 2011; Hayward et al., 2014). Yesuf et al. (2014) also showed that AGN are more commonly hosted by post starburst galaxies, with the peak AGN activity appearing $\geq 200 \pm 100$ Myr after the starburst. Such a SFH is not accounted for in the models presented here, however this scenario is still consistent with the results presented in this paper; that AGN which are *currently* active have been detected in host galaxies ~ 1 Gyr after the onset of quenching.

This rapid quenching is particularly dominant for low-to-medium mass smooth galaxies. Smethurst et al. (2015) suggest that incredibly rapid quenching rates could be attributed to mergers of galaxies in conjunction with AGN feedback, which are thought to be responsible for creating the most massive smooth galaxies (Conselice et al., 2003; Springel et al., 2005; Hopkins et al., 2008). This dominance of rapid quenching across the smooth AGN-HOST population supports the idea that a merger, having caused a morphological transformation to a smooth galaxy, can also trigger an AGN, causing feedback and cessation of star formation (Sanders et al. 1988).

Within the medium mass AGN-HOST population we see a bimodal distribution between these two quenching histories, highlighting the strength of this method which is capable of detecting such variation in the SFHs within a population of galaxies.

Indeed not all galaxies in the AGN-HOST and INACTIVE samples are quenching, as seen in Figure 4.3, with a significant proportion of both the AGN-HOST and INACTIVE samples lying on the star forming sequence. A galaxy can therefore still maintain star formation whilst hosting an AGN. The results presented in Section 4.1.2 only reflect the trends for galaxies that have undergone or are currently undergoing quenching within a population and can therefore be accurately fit by an exponentially declining

SFH. This prevalence of star forming AGN host galaxies, combined with the results above allows us to consider that either: (i) the AGN are the cause of the rapid quenching observed but only in gas-poor host galaxies where they can have a large impact, (ii) the AGN are a consequence of another quenching mechanism but can also be triggered by other means which do not cause quenching, or (iii) the SFR of a galaxy can recover post-quench and return to the star forming sequence after a few Gyr (see recent simulations by Pontzen et al. 2016). Further investigation will therefore be required to determine the nature of this quenching.

4.2 Bulgeless galaxies hosting growing black holes

The work in the following chapter has been submitted to MNRAS in Simmons, Smethurst & Lintott (subm.). I was responsible for the data reduction, statistical analysis and assisted in the interpretation.

In Section 4.1, I showed how disc galaxies currently hosting an AGN could have started quenching at early times. This secular co-evolution of the galaxy and black hole has been proposed before and investigated in ? with AGN which reside in disk dominated hosts whose accretion histories are assumed to be merger free. In the following work we investigate a larger sample of disc galaxies identified as bulgeless or disk dominated with an AGN and measure their black hole masses.

4.2.1 Observational Data

The goal of this study is to investigate black hole growth in galaxies whose growth histories have been dominated by relatively calm processes. We therefore require a sample of growing black holes hosted in disk-dominated galaxies. Optimally, the AGN should have broad emission lines to facilitate measurement of black hole masses via well-established relations between line flux and width and black hole masses. Previously, Simmons et al. (2013) investigated a sample of 13 pure disk galaxies hosting AGN. The selection method used in that study selected against very massive black holes with unobscured emission: only 2 AGN of 13 show clear signs of broadened line emission in their SDSS spectra, with masses of 4×10^6 and $1 \times 10^7 M_\odot$. Here we aim to select AGN at all masses but with broad emission lines, and which are hosted in disk-dominated galaxies. Below we describe the method used to select this sample and the data sets from which the sample is drawn.

4.2.1.1 AGN Selection

Examining the black hole-galaxy relation requires selection of a sample of unobscured AGN with broad emission lines, so that black hole masses may be measured from well-established correlations between emission line properties and black hole masses (e.g., Jiang et al., 2011; ?).

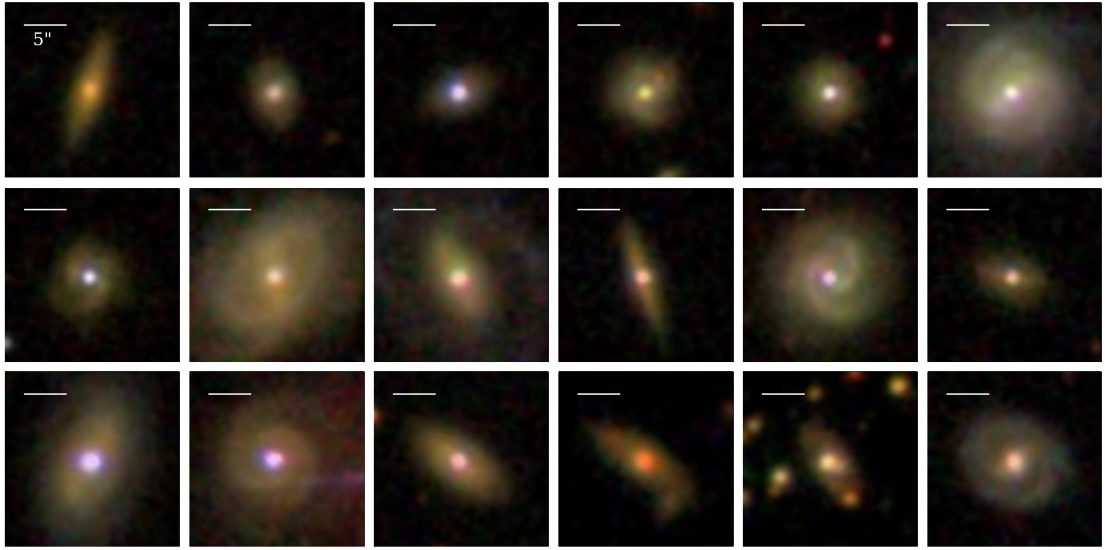


Figure 4.6: Example postage stamp SDSS images of galaxies within the sample of 101 bulgeless galaxies for which we have spectra. The last 5 images on the bottom row are the galaxies observed with the IDS on the INT. The scale for each image is shown by the 5'' ruler in each panel.

Unobscured AGN have characteristic colours in multi-wavelength imaging, particularly in X-ray, optical and infrared bands (???). Given the existence of all-sky surveys at many of the wavelengths relevant to the selection of unobscured AGN, it is now possible to construct samples of sources identified as unobscured AGN with high likelihood.

We select an initial sample of AGN using the W2R sample of ?, comprised of 4316 sources identified using multi-wavelength data from the *Wide-field Infrared Survey Explorer* (*WISE*; Wright et al., 2010), Two Micron All-Sky Survey (2MASS; ?), and *ROSAT* all-sky survey (RASS; ?). This is a photometric, all-sky selection, which selects unobscured AGN at > 95 per cent confidence ?.

4.2.1.2 Selecting disk-dominated AGN host galaxies

Following the AGN selection described above, we further sub-select galaxies imaged by the Sloan Digital Sky Survey. There are 1,844 W2R sources with positional matches having reported coordinates within 3'' of a source in SDSS (York et al., 2000) Data Release 8 (?), a fraction consistent with the fractional area of the SDSS versus an

all-sky catalog. 76 per cent of this sub-sample has measured redshifts, with a peak redshift distribution of $z \approx 0.12$. 90 percent of sources with redshifts have $z < 0.6$; the distribution has a long tail to $z_{\text{max}} = 2.35$.

We then examine each SDSS colour cutout to identify disk-dominated features. One author (BDS) identified ??? (SDSS+13+INTB) disk-dominated AGN host galaxies on the basis of clearly identifiable spiral arms, bars or obvious edge-on disks. Figure 4.2.1.2 shows a sample of these galaxies.

4.2.1.3 Spectra

Of the ??? disk-dominated AGN host galaxies with SDSS imaging observations, 73 have spectra from SDSS Data Release 9 (?). The others are not included because they lie outside the Data Release 7 footprint (which had high spectral completeness) and were not targets for any SDSS-III projects (which have specific requirements and generally do not include AGN host galaxies with low enough redshift to identify spiral arms in SDSS imaging). [23 also have spectra and were identified from Chen and Edelson & Malken.](#) We measured the broad $H\alpha$ emission for [5 additional sources](#) using long-slit spectra using IDS on INT from 21st-23rd May 2014. Spectra were reduced using the standard reduction pipeline of Massey, Valdes & Barnes (1992) using IRAF modules to debiased, dark subtract, flat field, calibrate, sky subtract, flux calibrate and extract spectra. These reduced spectra are shown in Figure 4.2.1.3 for the 5 galaxies observed.

Figure 4.2.1.3 shows the redshift distribution of all 101 sources for which we have spectra; the mean redshift of the sample is $\langle z \rangle = 0.129$, with the highest-redshift source having $z = 0.244$.

4.2.2 Stellar and Black Hole Masses

[Probably want a short intro paragraph here. We compute masses because we want to explore co-evolution, below we describe how we do that. etc. Just something to keep the narrative going and prevent the section and subsection headings from colliding.](#)

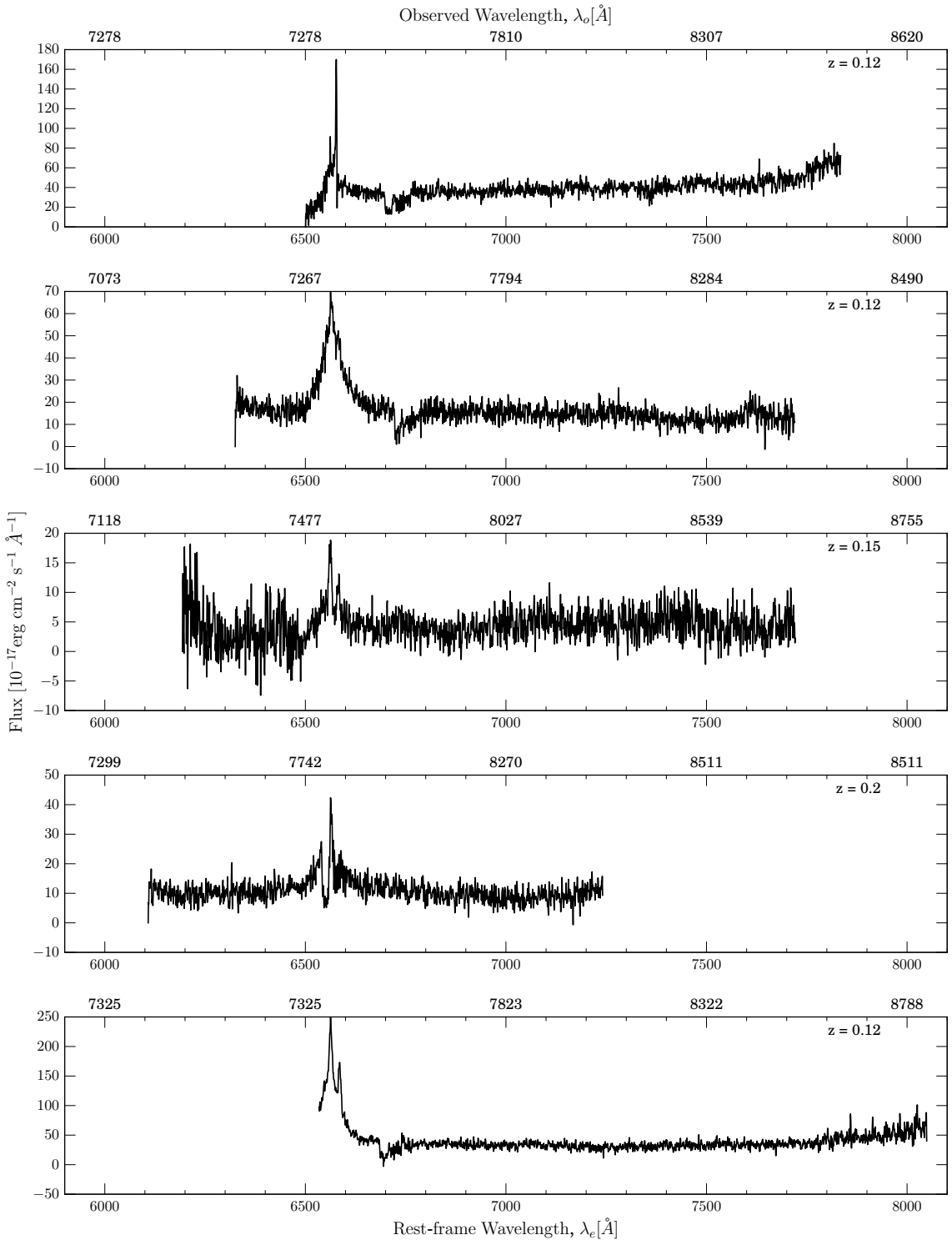


Figure 4.7: Reduced spectra from the IDS on the INT for the 5 galaxies observed with the corresponding measured redshift values shown. Each panel shows the same rest-frame wavelength range (bottom axis of each panel); observed wavelengths are shown on the top axis of each panel, with redshifts in the top right of each panel. All spectra show broadened H α emission, confirming that the multi-wavelength AGN selection employed here efficiently selects 53 obscured AGN.

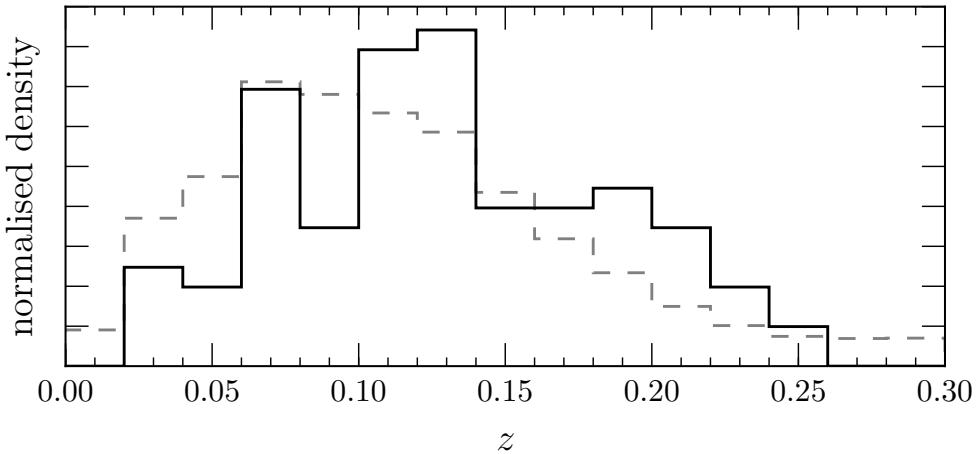


Figure 4.8: Normalised redshift distribution for all 101 sources (solid) for which we have spectra, either from SDSS or measurements with the IDS on the INT. Also shown is the overall redshift distribution of SDSS DR7 in the relevant redshift range of our sources (dashed).

4.2.2.1 Galaxy and bulge stellar masses

We calculate stellar masses using the well-studied relation between stellar mass, absolute galaxy r -band magnitude, and $u - r$ galaxy colour (corrected for galactic extinction; ?), following the method of ?. We remove the AGN contribution to the luminosity and colour of each galaxy by subtracting the flux in the SDSS `psfMag` from the flux in `modelMag`. `psfMag` is the best estimate of unresolved emission, while `modelMag` is the optimal quantity for computing aperture-matched source colours¹.

The full sample of total stellar masses spans the range from $7 \times 10^9 M_\odot < M_* < 2 \times 10^{11} M_\odot$, with a mean galaxy stellar mass of $12345 M_\odot$. Each individual mass has an uncertainty of 0.3 dex from the scatter in the colour-luminosity relation, with typically an additional $????$ uncertainty due to the AGN subtraction (dependent on the nuclear luminosity, e.g. Simmons & Urry, 2008). The typical combined uncertainty in the stellar mass is $????$ dex.

The nuclear emission, as estimated via comparison of `psfMag` to `modelMag`, is generally between 20 to 200 per cent of the galaxy-only emission. The presence of the luminous AGN severely compromises the estimates of the bulge-to-total ratio in the

¹<https://www.sdss3.org/dr10/algorithms/magnitudes.php>

host galaxy provided by, e.g., the `fracDeV` parameter reported in the SDSS catalogs. That parameter estimates that 80 per cent of the galaxies in this sample are pure de Vaucouleurs (1953) bulges in the r -band, despite the fact that the sample was selected on the basis of clear visual signatures of dominant disks (Figure 4.2.1.2). None of the photometric parameters measured by the SDSS pipeline allow for the dual presence of an AGN and a host galaxy; without such considerations the unresolved AGN light is likely to be attributed to the compact bulge component in a bulge-disk model fit (Simmons & Urry, 2008; ?; Koss et al., 2011).

AGN-host decomposition based on 2-dimensional image fitting (e.g., Peng et al., 2002, 2010; ?) is more reliable (e.g. McLure et al., 1999; Urry et al., 2000; McLure & Dunlop, 2001; Sánchez et al., 2004; Pierce et al., 2007; Gabor et al., 2009; ?; ?; Simmons et al., 2013; Koss et al., 2011; ?), although even in high-resolution *Hubble Space Telescope* (*HST*) images (Simmons & Urry, 2008; ?) or SDSS imaging at $z \gtrsim 0.06$ (Koss et al., 2011; Simmons et al., 2013) the recovered bulge-to-total ratio can be highly uncertain, particularly for disk-dominated galaxies with a small bulge or pseudo-bulge component. While the AGN-host decompositions of the sample of Simmons et al. (2013) recovered reliable parameters to compact pseudo-bulge components for 11 of 13 galaxies, those sources are at substantially lower redshift than this sample, and their AGN are significantly less luminous ([quantify this more](#)).

We undertook a similar procedure as in that study to attempt bulge-to-total fits to 5 exemplar galaxies in this sample (Figure 4.2.1.2), with a median redshift of $z = 0.13$ and typical r -band nuclear fluxes [approximately equal to the total galaxy \$r\$ -band flux](#). We recovered stable, but highly uncertain, bulge-to-total ratios for only 2 of the 5 galaxies; in the remaining cases the nuclear emission is too bright and the resolution too low for a reliable bulge-to-disk decomposition. Detailed AGN-host fits to the SDSS images in the entire sample are not likely to produce useful measurements of bulge masses; *HST* imaging, which would enable this, is currently not available for the galaxies in this sample.

Nevertheless, it is possible to constrain the bulge contribution to the host galaxies using existing structural parameters from large-scale studies performing bulge-disk decompositions of SDSS galaxies. While such studies do not account for the presence of an AGN, their tendency to overestimate the bulge-to-total ratio as a result means that bulge masses derived from these quantities may be taken to be conservative upper limits.

We use the bulge-disk decompositions of Simard et al. (2011), who fit multiple models to 1.12 million galaxies in the SDSS catalog and determined best-fit models and structural parameters for each. We take the r -band bulge-to-total ratio [of the best-fit model](#) as an upper limit to the true bulge-to-total ratio of these AGN host galaxies. To convert limits on bulge luminosities to limits on bulge masses, we assume the mass-to-light ratio of the bulge is equal to the mass-to-light ratio of the disk. In disk-dominated galaxies, where many of the “bulge” components are likely to be rotationally-supported pseudo-bulges (Kormendy & Kennicutt, 2004) whose stellar populations are similar to that of the disk ([e.g., Graham, 2001; ?](#)), this is a reasonable assumption.

The upper bulge-to-total limits of the 89 galaxies in this sample which were included in the Simard et al. study range from $0.13 \leq (B/\text{Tot})_{\text{max}} \leq 1.0$, [with a mean value of 0.5](#). Applying these bulge-to-total limits to the stellar masses computed using the colour-luminosity relation (Bell & de Jong, 2001; ?) results in bulge mass upper limits of $3 \times 10^9 M_\odot < M_{\text{bulge}} < 7 \times 10^{10} M_\odot$. These mass limits will be compared with black hole masses for the sample in Section 4.2.3.

4.2.2.2 Black hole mass estimates

The selection of unobscured AGN facilitates accurate estimates of black hole masses. Unobscured AGN have broad emission lines originating from within the black hole sphere of influence, which can be used to estimate the velocity of the orbiting broad-line clouds and the radius of the emitting region (??). Each AGN in the sample has 1 spectrum, meaning the broad-line-derived black hole masses are “single-epoch”, relying on simplifying geometric assumptions and empirically established relationships between observed and physical quantities to compute masses using the virial theorem (??). Single-epoch black hole mass estimates are more uncertain than those derived from reverberation mapping and other more precise methods (??), but they are considerably more accurate than many other methods ([e.g., Eddington-based estimates](#)). We use the established relation between black hole mass and the FWHM and luminosity in the broad H α line (Greene & Ho, 2007).

We perform spectral fitting on each of the SDSS and INT spectra described in Section 4.2.1.3 to recover narrow-line strengths and broad-line strengths and widths to the H α 6563 Å line, using **GANDALF** (Sarzi et al., 2006) [to fit multiple simultaneous](#)

lines as well as the continuum. GANDALF is optimised for use with SDSS spectra; using the program with the INT spectra required minimal data re-formatting: we binned logarithmically and de-redshifted the spectra. From the continuum-subtracted best fit, we determine the FWHM and line flux of the broad H α line simultaneously with the narrow H α component via `emcee`², a Python implementation of a Markov Chain Monte Carlo (MCMC; Mackay, 2003; ?) affine invariant ensemble sampler by Foreman-Mackey et al. (2013).

The uncertainties reported by `emcee` are limited to those from the separation of narrow and broad line components in measurement of the FWHM. We also determine uncertainties from the GANDALF fits using a bootstrap method sampling within the spectral noise and re-fitting with $N = 1000$ iterations for each spectrum. The reported uncertainties on black hole masses include both these sources of uncertainty as well as the reported uncertainties in the black hole-broad line relation (Greene & Ho, 2007). There are other sources of uncertainties, such as those involved in implicitly assuming a fixed geometric correction factor f for each SMBH, and the error introduced by assuming a Gaussian line profile for all measured broad lines. Determining uncertainties for the former is outside the scope of this study; based on visual inspection of the line fits the latter is very small (not sure how to estimate how small? Could try it out on the fits with the worst non-artifact residuals?) compared to the other uncertainties. The fits to the INT spectra are shown in Figure 4.9.

The black hole masses for the sample of ??? galaxies range from $10^6 M_\odot \leq M_{\text{BH}} \leq 2 \times 10^9 M_\odot$. The median mass is $3 \times 10^7 M_\odot$. We compare these to galaxy stellar masses and bulge mass upper limits in Section 4.2.3.

4.2.3 Galaxy-Black Hole Mass Relations

The total stellar mass (estimated bulge masses - see Section 4.2.2.1) and black hole masses of the 101 galaxies in our sample are shown in the left (right) panel of Figure 4.2.3. We fit a linear regression model to both of these relations using a Bayesian method which encompasses both the two-dimensional uncertainties on each measurement and the intrinsic scatter in the data. This method is outlined in ? and is publicly available as a *Python* module LINMIX³. For the bulge mass in the right panel

²dan.iel.fm/emcee/

³<http://linmix.readthedocs.org/>

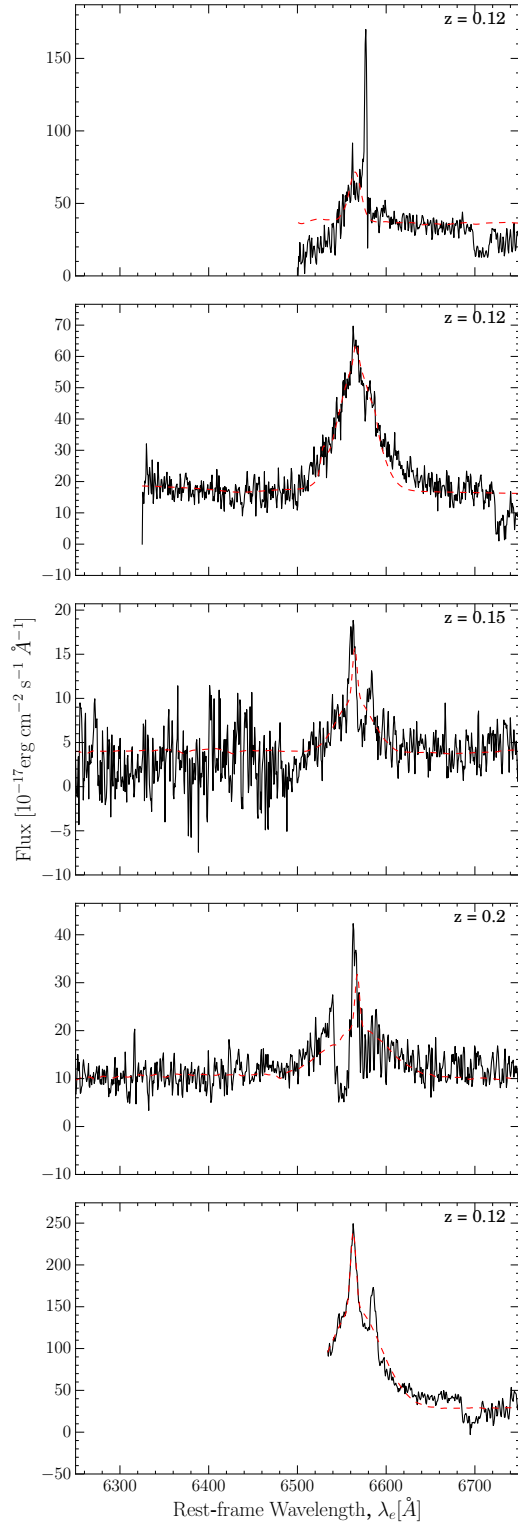


Figure 4.9: Reduced spectra from the IDS on the INT for the 5 galaxies observed with the corresponding measured redshift values shown. Spectra are aligned with the broad $H\alpha$ emission line, the gaussian fits to which are shown by the dashed red line.

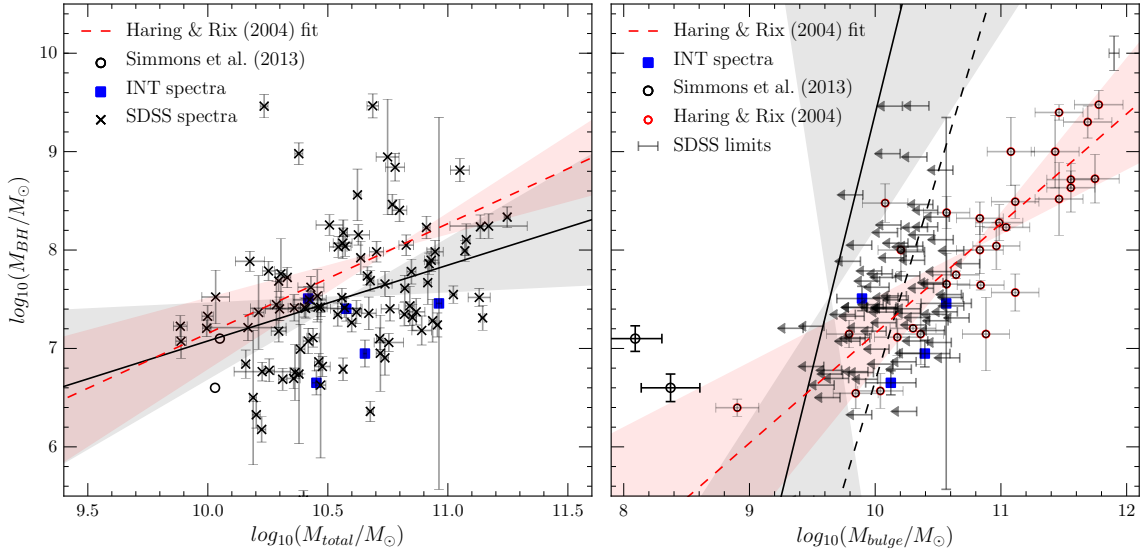


Figure 4.10: Total stellar mass against the black hole mass (left) of the 101 galaxies, including those observed by SDSS (crosses), with the IDS on INT (blue squares) and detections from Simmons et al. (2013, open circles). The best fit line to the data points and two-dimensional errors from linear regression is shown (solid line) with $\pm 3\sigma$ (grey shaded). For 89 of the galaxies we have upper limits (black arrows) on the $(B/T)_g$ ratio from which we can determine an upper limit on the stellar bulge mass. We plot this value against the black hole mass (right) and show the best fit to these upper limits and two-dimensional errors using linear regression methods (solid line) with $\pm 3\sigma$ (grey shaded). The dashed line shows the fit if the upper limits are not treated as such. In both panels we also show the best fit found using this same method to the early-type galaxies of Häring & Rix (2004) (dashed line) with $\pm 3\sigma$ (red shaded) and the measured values shown by the red circles. Despite the fact that these galaxies are predominantly disk dominated they will are most likely to lie above the Häring & Rix (2004) relationship found for bulge dominated systems (see discussion in Section 4.2.3).

of Figure 4.2.3 this method can also incorporate the upper limits on the measurements for the 89 SDSS galaxies (see Section 4.2.2.1).

Using this same method, we fit to the observations of 30 early-type galaxies from Häring & Rix (2004). Despite the fact that our sample of galaxies is disk dominated and contain either a pseudo-bulge or no bulge, they most likely lie above the relationship derived using the bulge dominated galaxies of Häring & Rix (2004).

We consider how the black hole mass compares to the Eddington ratio, or accretion rate of these disk dominated galaxies and compare with a redshift matched subsample of 198 galaxies in the DR7 quasar sample from Shen et al. (2011). This is shown in Figure 4.11. The 101 galaxies in our disk dominated sample have both lower black hole masses and lower bolometric luminosities in comparison to the Shen et al. (2011) sample, however the Eddington ratio's are very similar, see Figure 4.12. In fact, the Eddington ratio's of the redshift matched sample are on average, lower than that for the disk dominated sample. We can reject the null hypothesis that the disk dominated galaxies are drawn from the same distribution as the redshift matched quasar sample from Shen et al. (2011) but not for the entire quasar sample of Shen et al. (2011).

'ERE BE SCIENCE!

Within this redshift matched sample, 108 galaxies were morphologically classified by the Galaxy Zoo 1 project Lintott et al. (2008); ?, all of which have a debiased combined spiral vote fraction (Galaxy Zoo 1 did not ask whether a galaxy was a disk, therefore we can approximate the combined spiral vote fraction as a disk vote fraction) of $p_{CS} < 0.5$ and mean value of $\langle p_{CS} \rangle = 0.17$.

Slightly higher accretion rates are therefore occurring in the AGN of these disk dominated galaxies than in a bulge dominated quasar sample from SDSS. **'ERE BE SCIENCE!.**

4.2.4 Discussion

- Eddington ratios - use WISE W3 for Lbol and compare with BH masses to talk about Eddington ratios of the sample in Figure 4.11.
- Do the Lbol or Eddington ratios or masses look different for disk-dominated hosts in clear interactions?

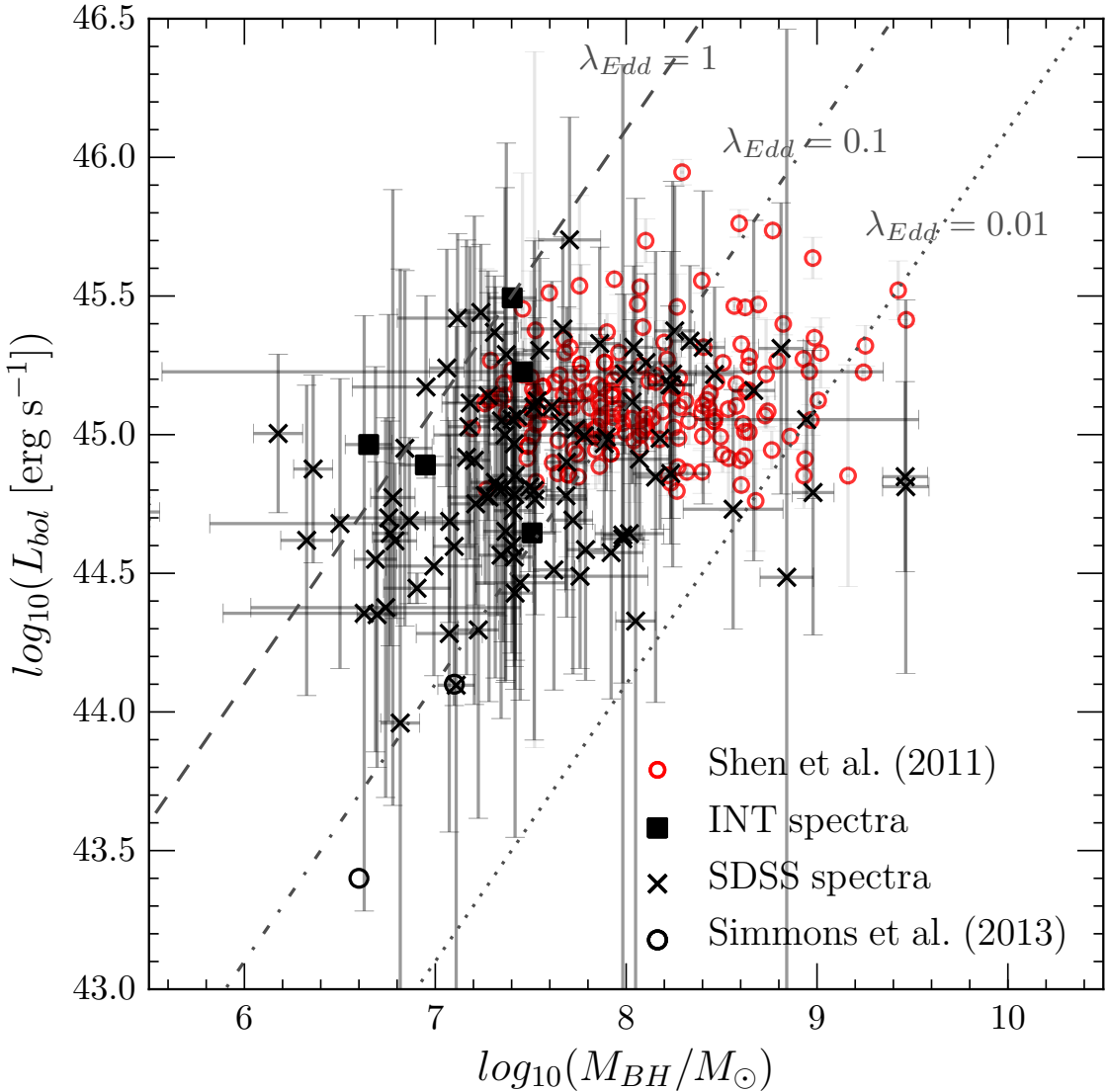


Figure 4.11: Black hole mass against bolometric luminosity for the 101 galaxies, including those observed by SDSS (crosses) and with the IDS on INT (squares). We also show detections from [Simmons et al. \(2013\)](#) (open circles) and those from the redshift matched sample of [Shen et al. \(2011\)](#). For reference we show lines of example Eddington ratios of $\Lambda_{Edd} = 1$ (dashed), $\Lambda_{Edd} = 0.1$ (dot-dashed) and $\Lambda_{Edd} = 0.01$ (dotted).

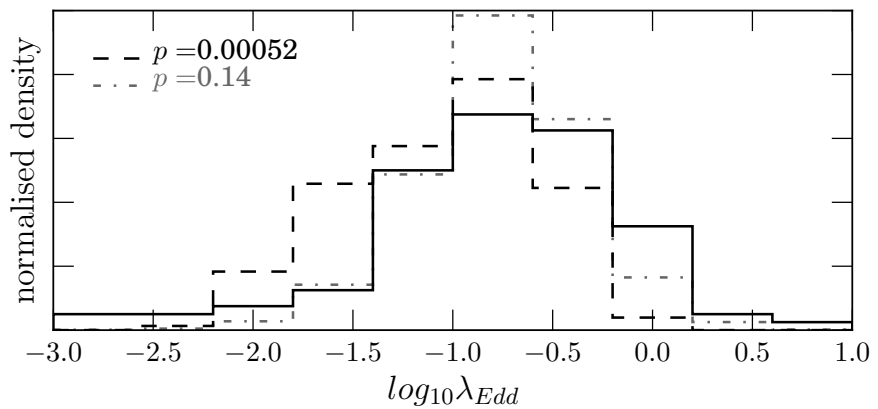


Figure 4.12: Normalised distributions of logarithmic Eddington ratio for the sample of 101 disk dominated galaxies (solid line), compared with that for the redshift matched sample from Shen et al. (2011; dashed line) and the entire sample (dot-dashed line). We also provide the p-values of a 2 sample KS test between the disk dominated sample and each of the quasar samples. We reject the null hypothesis that the two samples are drawn from the same population for the redshift matched quasar sample but accept the null hypothesis for the entire quasar sample of Shen et al. (2011).

Chapter 5

The influence of the group environment

5.1 Group Identification

We used the Berlind et al. (2006) catalogue, which uses a friends-of-friends algorithm to identify group and cluster galaxies in the SDSS. This was cross matched to the GZ-GALEX sample and limited to $z < 0.1$ to ensure GALEX completeness of the red sequence (see ?). Centrals were selected as the brightest galaxy in a group and all others were designated as satellites. This resulted in a sample of 14,199 group galaxies with 3,468 centrals and 10,731 satellites within a projected cluster centric radius range of $0 < R/R_{200} < 25$ and $z < 0.084$.

In this work we focus on galaxies which are either quenching or quenched and are more than $\pm 1\sigma$ below the star forming ‘main sequence’. This encompasses 4629 satellite and 2314 central galaxies and will be referred to as the GZ-GROUP sample. These galaxies are highlighted in red on Figure ??.

5.1.1 Field sample

For all galaxies in the GZ-GALEX sample, we calculated the smallest projected cluster centric radii from each of the central galaxies in the Berlind et al. (2006) catalog and selected candidate field galaxies as those with (i) $R/R_{200} > 25$ and (ii) $\log \Sigma < -0.8$

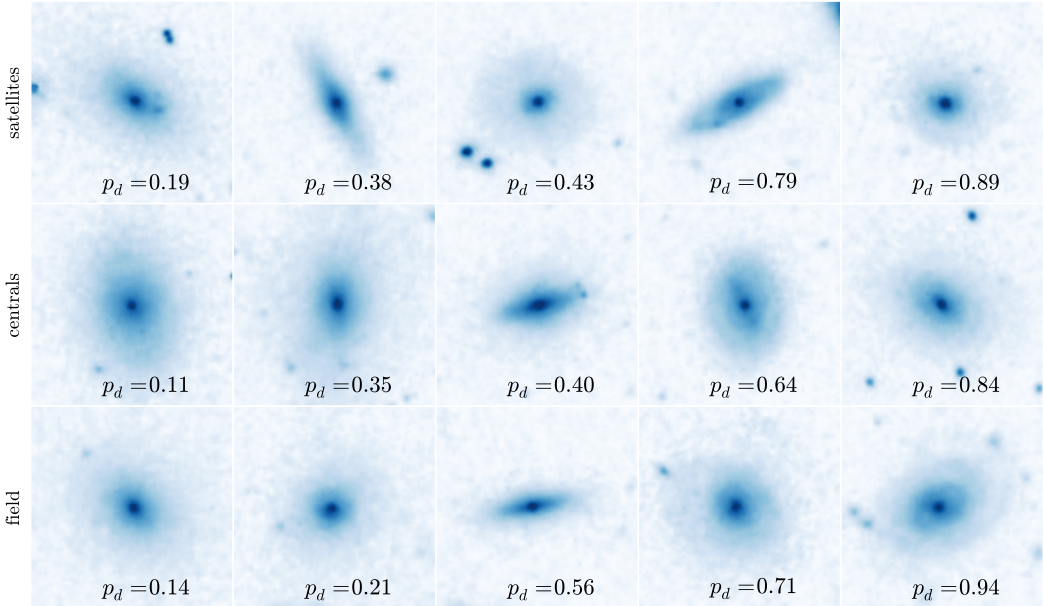


Figure 5.1: Randomly selected SDSS *gri* composite images of satellite and central galaxies in the GZ-GROUP sample in comparison to those from the GZ-FIELD sample. All galaxies lie within $0.04 < z < 0.05$ and in the central galaxy mass range $10^{10.5} < M_*(M_\odot) < 10^{11}$, used as a proxy for halo mass. The galaxies are ordered from least to most featured according to their debiased ‘disc or featured’ vote fraction, p_d (see Willett et al. 2013). The scale for each image is 0.099 arcsec/pixel.

from ?. This sample of field galaxy candidates was then matched in redshift and stellar mass firstly to the central galaxies of the GZ-GROUP sample to give 2,309 field galaxies with $z < 0.084$ which will be referred to as the GZ-CENT-FIELD sample. Secondly, the field galaxy candidates were then matched in redshift and stellar mass to the satellite galaxies of the GZ-GROUP sample to give 6,849 field galaxies with $z < 0.084$ which will be referred to as the GZ-SAT-FIELD. These galaxies in the GZ-SAT-FIELD sample will be used as a control when investigating the morphological trends of satellite galaxies with environment.

As in Section 5.1 we select all those galaxies in the central matched sample $\pm 1\sigma$ below the star forming ‘main sequence’, giving 1596 quenching or quenched field galaxies for use as a control sample, which will be referred to as the GZ-CENT-FIELD-Q sample. These galaxies will be used as a control when investigating the quenching parameters of the different environments in order to ensure that each galaxy under comparison resides in similar stellar mass halos.

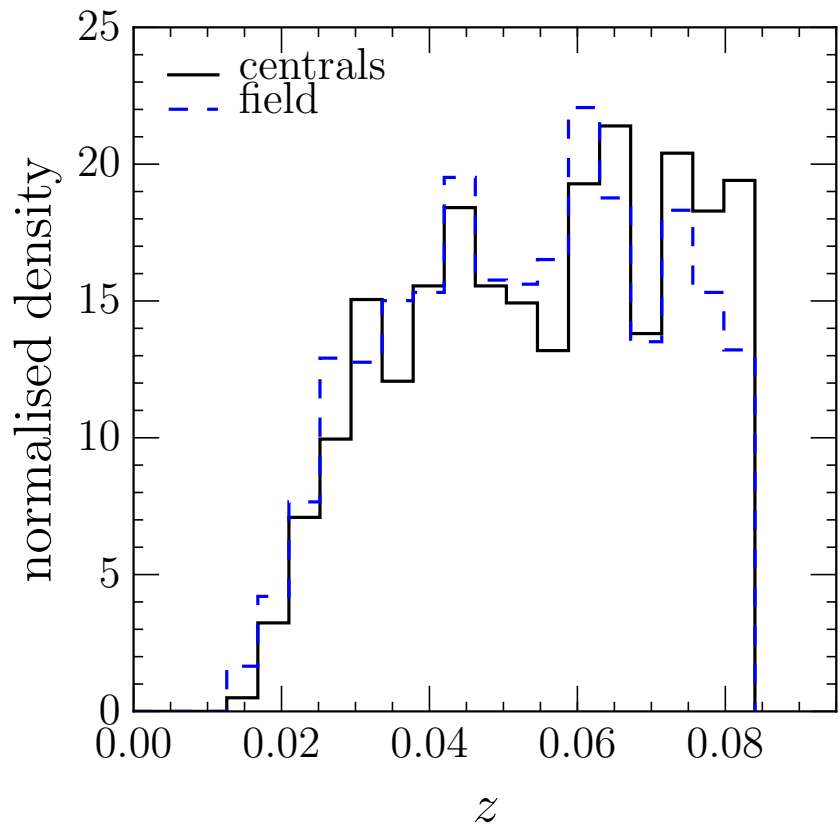


Figure 5.2: Redshift distributions of quenching or quenched central galaxies in the GZ-GROUP sample (black solid line) in comparison to the redshift and mass matched GZ-CENT-FIELD-Q sample (blue dashed line).

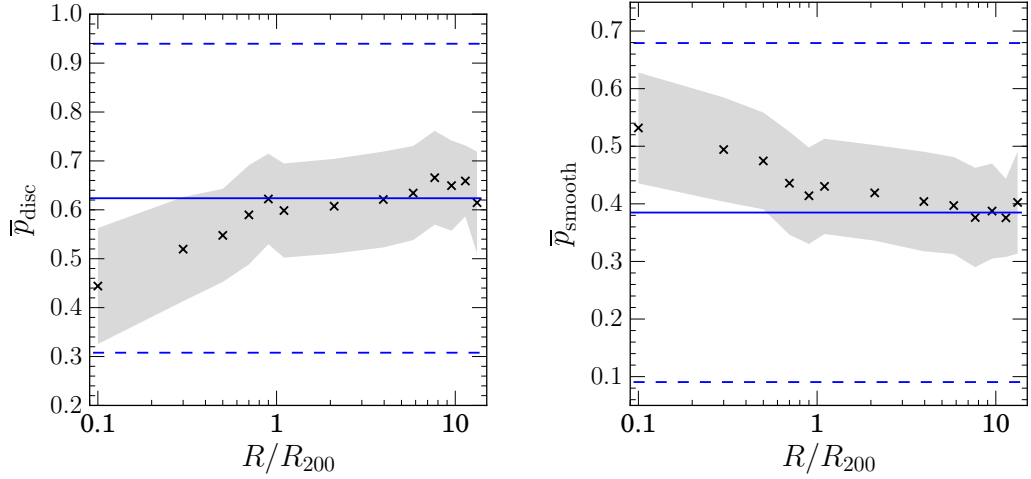


Figure 5.3: Mean GZ vote fraction for disc (top) and smooth (bottom) galaxies in the GZ-GROUP sample binned in projected cluster centric radius, normalised by R_{200} , a proxy for the virial radius of a group. The shaded region shows $\pm 1\sigma$ on the mean vote fraction. The mean vote fraction of the FIELD sample are also shown (blue solid lines) with $\pm 1\sigma$ (blue dashed lines).

5.2 Results

With the output from STARPY we can also study the time since quenching onset ($\Delta t = t_{obs} - t_q$, see Section ??) binned in projected cluster centric radius, normalised by R_{200} (a proxy for virial radius) for satellite galaxies and central galaxies in the GZ2-GROUP sample, compared with galaxies in the GZ2-FIELD sample. We can investigate these trends with group properties as shown in Figures 5.8 & 5.9.

Across all the panels in Figures 5.8 & 5.9 we see a general trend for increasing time since quenching onset with decreasing distance from the group centre, which is suggestive that this trend is due to an environmental quenching mechanism. As earlier, in Figures 5.3–5.6 significant differences from the field value arise inside \sim one virial radius.

If mergers are an important evolutionary mechanism for satellite galaxies as the morphological evidence in Figures 5.2 & 5.6 suggests, we would expect to see a difference in the quenching histories of satellites in groups with a higher number of galaxies, N_{group} . However, the bottom panel of Figure 5.8 shows that there is no trend with time since quenching onset with increasing N_{group} for the satellite galaxies. The cen-

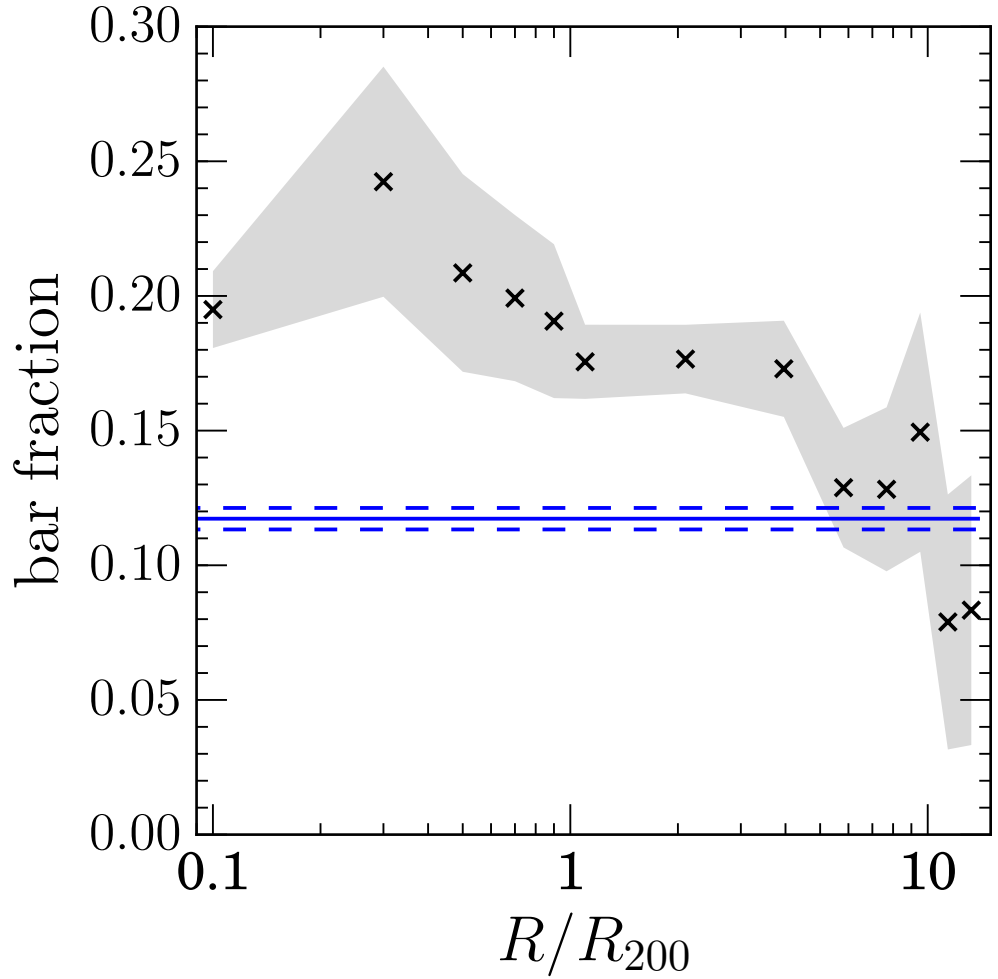


Figure 5.4: Bar fraction (number of barred disc galaxies over number of disc galaxies) in the GZ-GROUP sample binned in projected cluster centric radius, normalised by R_{200} , a proxy for the virial radius of a group. The shaded region shows $\pm 1\sigma$ on the bar fraction. The bar fraction of the GZ-SAT-FIELD sample is also shown (blue solid line) with $\pm 1\sigma$ (blue dashed line).

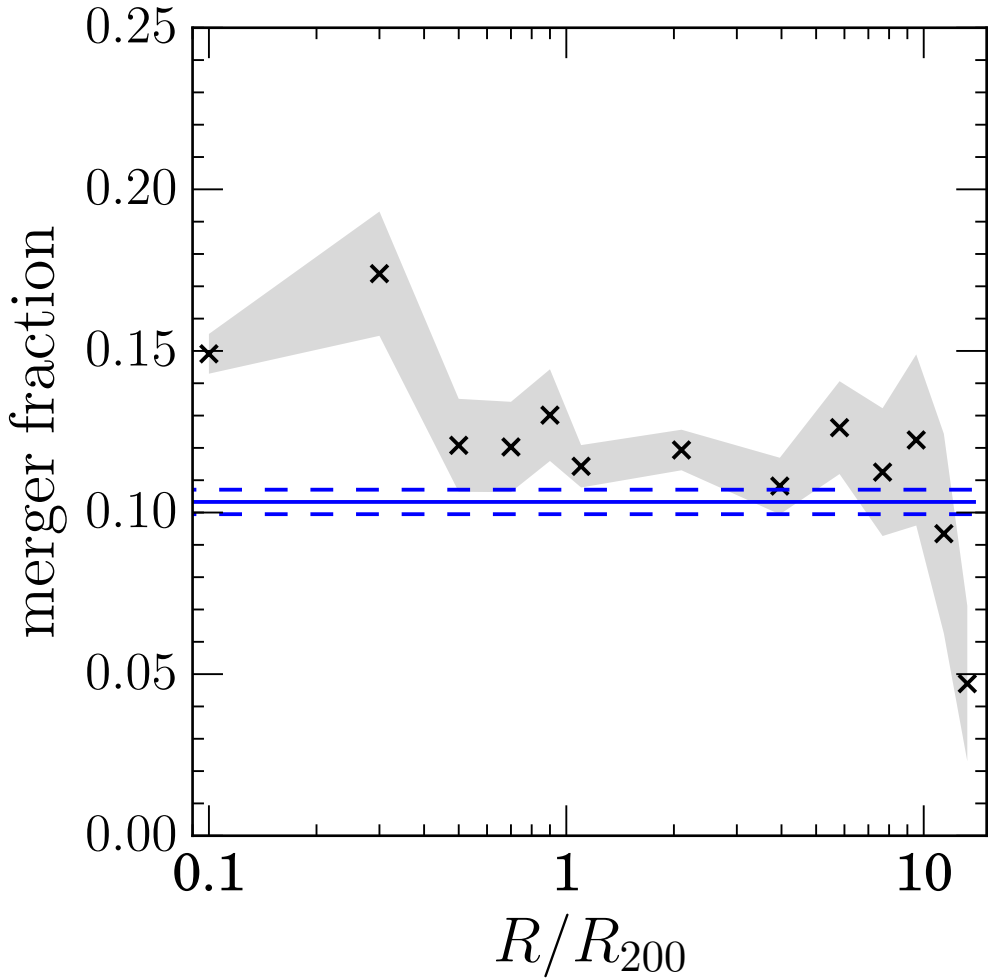


Figure 5.5: Merger fraction in the GZ-GROUP sample binned in projected cluster centric radius, normalised by R_{200} , a proxy for the virial radius of a group. The shaded region shows $\pm 1\sigma$ on the merger fraction. The merger fraction of the GZ-SAT-FIELD sample is also shown (blue solid line) with $\pm 1\sigma$ (blue dashed line).

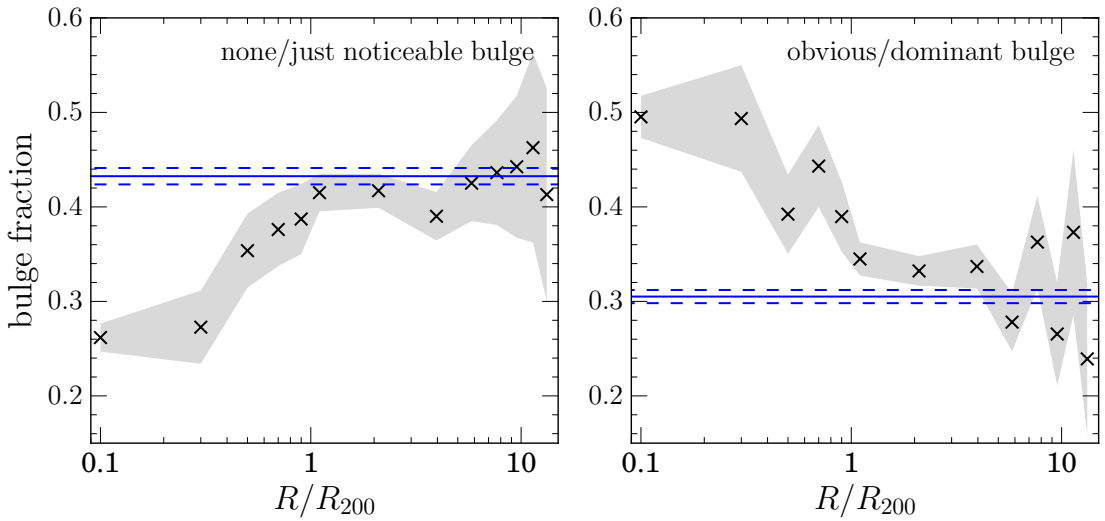


Figure 5.6: Fraction of galaxies with none/just noticeable bulge classifications (left) and with obvious/dominant bulge classifications (right) in the GZ-GROUP sample binned in projected cluster centric radius, normalised by R_{200} , a proxy for the virial radius of a group. The shaded regions shows $\pm 1\sigma$ on the bulge fractions. The bulge fractions of the GZ-SAT-FIELD sample are also shown (blue solid lines) with $\pm 1\sigma$ (blue dashed lines).

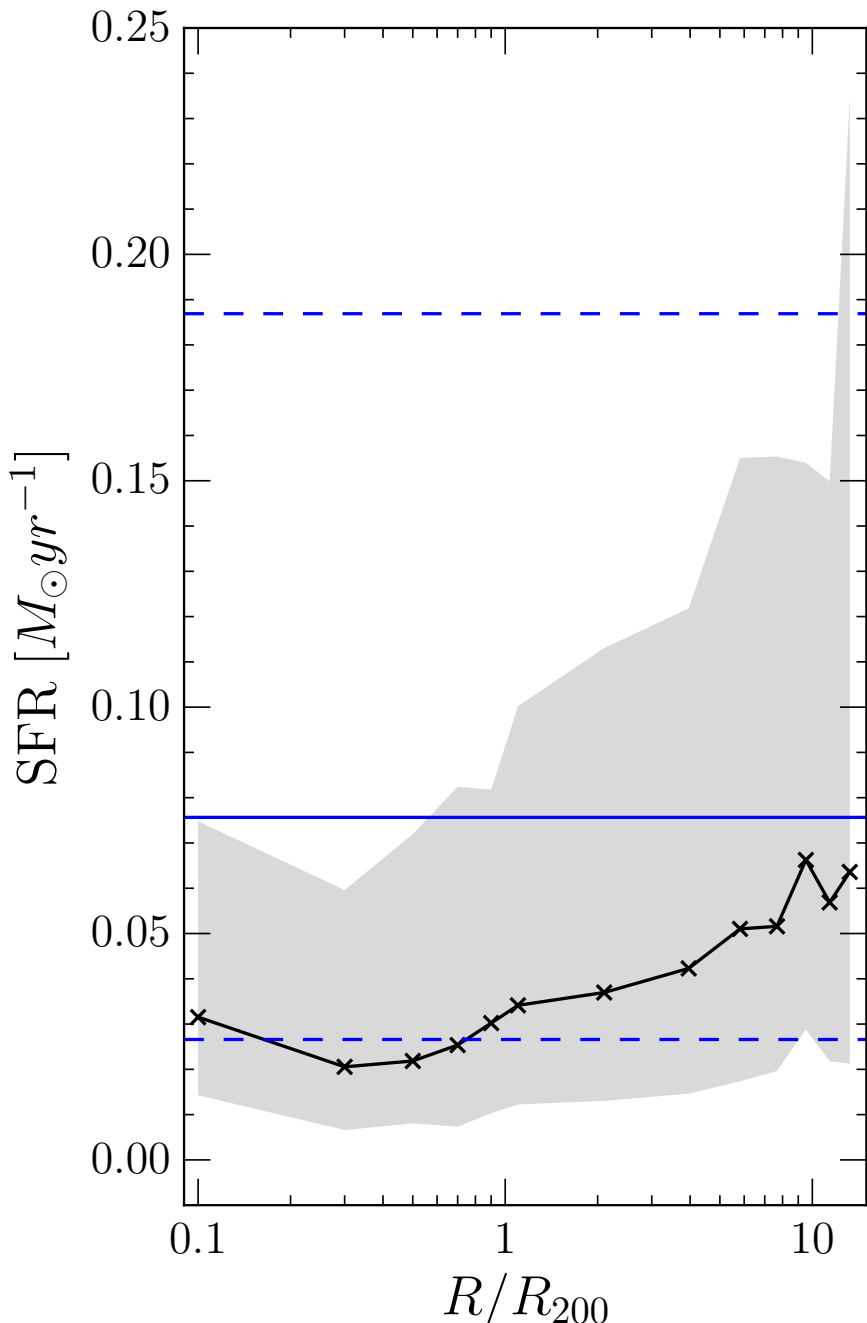


Figure 5.7: Median $H\alpha$ derived star formation rates of satellite galaxies in the GZ-GROUP sample, binned in projected cluster centric radius, normalised by R_{200} , a proxy for the virial radius of a group. The shaded region shows the SFRs encompassed by 50% of the population in a given bin. The median SFR of the GZ-SAT-FIELD sample is shown (blue solid line) along with the 25th and 75th percentiles (blue dashed lines).

tral galaxies (shown by the square points at $\sim 0.01R/R_{200}$) however, do show a trend for increasing time since quenching with N_{group} . Suggesting that mergers are not the dominant quenching mechanism for satellite galaxies but are for centrals.

In the middle panel of Figure 5.8 the satellite galaxies of the GZ2-GROUP sample are now split by their stellar mass (calculated from the absolute r-band magnitude and $u - r$ colour by the method outlined in ?) and we do see a clear trend for increasing time since quenching onset with increasing stellar mass for both satellite and central galaxies. This is suggestive of mass quenching among the group galaxy population. This is contrary to previous work suggesting that mass quenching is only of import for central galaxies (???). Interestingly, the inner satellites of a given mass have quenched less recently than the centrals at the same mass range, suggesting some episode of more recent star formation may have occurred in the central galaxies but not in the inner satellites. This is once again suggestive of a merger dominated evolutionary history for central galaxies, with mergers postulated to cause a burst of star formation before then quenching the remnant galaxy (??Pontzen et al., 2016).

In simulations, the three things that are found to most constrain galaxy evolution are redshift, mass and halo mass ???. To study the effect that halo mass has on the quenching properties of group galaxies we shall use a proxy for halo mass by splitting by the GZ2-GROUP sample by the stellar mass of the corresponding central galaxy of a group.

This is shown in the top panel of Figure 5.8 where we can once again see a clear trend for increasing time since quenching onset with increasing stellar mass of the group central for both satellite and central galaxies. More massive halos therefore have a greater impact on the star formation histories of their satellites than less massive halos. This is often though to be attributed to hotter inter galactic medium (IGM) temperatures in higher mass halos which can then impact on a galaxy through ram pressure stripping (RPS) of gas for star formation. If RPS is indeed a dominant environmental quenching mechanism we should therefore see a trend in Δt with the speed of a satellite galaxy relative to the group central. In the bottom panel of Figure 5.9 we split the satellite galaxies of the GZ2-GROUP sample into bins of relative velocity to their central galaxies. We can see that there is no trend with time since onset of quenching with increasing relative velocity for satellite galaxies, however the trend with decreasing projected group centric radius, seen in each panel in Figure 5.8

is still present. This suggests that any environmental processes causing this quenching are not corrected with satellite velocity and therefore RPS is not the dominant environmental quenching mechanism, in support of the conclusions of (?).

We can also account for both the stellar mass and the halo mass of the central galaxy simultaneously by considering the stellar mass ratio of the satellite to its central galaxy, $\mu_* = M_*/M_{*,c}$, once again using the stellar mass of the central galaxy as a proxy for halo mass. In the middle panel of Figure 5.9 we show the time since quenching of the GZ2-GROUP sample with projected cluster centric radius split into bins of μ_* . The change in Δt with projected cluster centric radius occurs more steeply (particularly beyond \sim a virial radius) for satellite galaxies with much smaller masses than their group central ($-2.0 < \log_{10} \mu_* < -1.0$, shown by the blue curve). Since the stellar mass of the central galaxy is correlated with the halo mass and therefore the potential of the system, this suggests that smaller mass galaxies in larger halos are most effected by environmental effects, therefore the dominant environmental quenching mechanism must be correlated with the group potential.

Previous studies have claimed that the property which correlates most with whether a galaxy is quenched is the stellar velocity dispersion, σ_* . Shown in the top panel of Figure 5.9 is the time since quenching of the GZ2-GROUP sample with projected cluster centric radius split into bins of σ_* . Along with the stellar mass (shown in the middle panel of Figure 5.8), the stellar velocity dispersion shows the largest trend in Δt for satellite galaxies, with galaxies with the smallest (largest) stellar velocity dispersions have quenched more (less) recently.

5.3 Discussion

Across all panels of Figures 5.8-5.9 a trend for increasing time since quenching onset with decreasing projected cluster centric radius was present. This suggests that the environment does directly cause quenching; galaxies closer in, fell into the group earlier and as they did so they started to quench giving rise to a larger Δt . However, as seen in Figure 5.9 there is no trend in the time since quenching onset with the relative velocity of the satellites to their corresponding central and a steeper trend with R/R_{200} for lower mass satellites in larger mass halos. This suggests that whatever environmental mechanism is at play here, it is dependant on the size of the halo, either

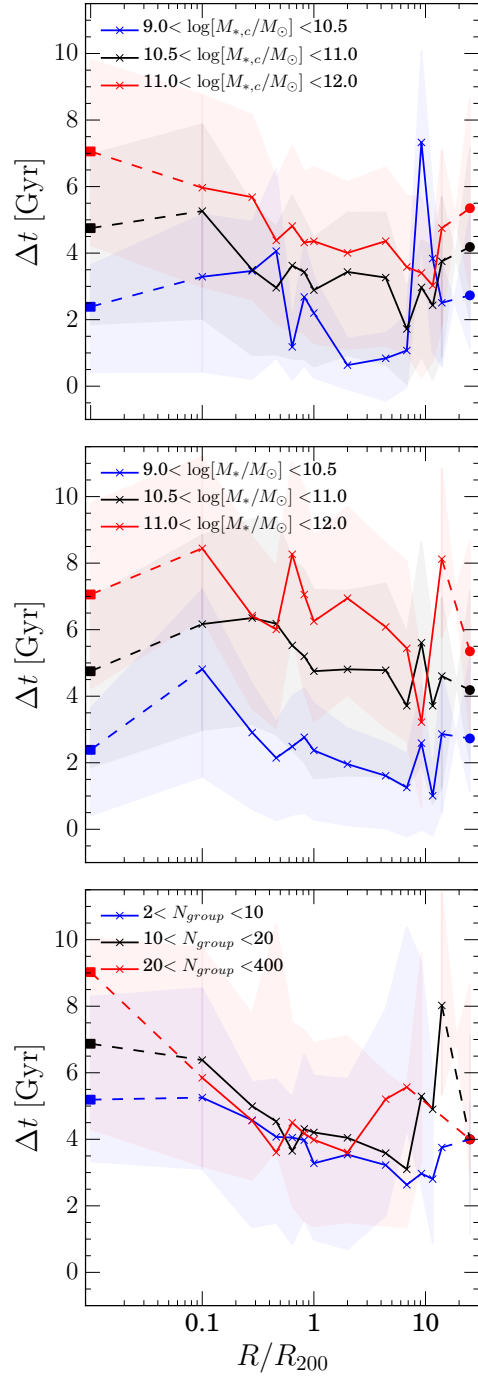


Figure 5.8: The time since quenching onset ($\Delta t = t_{obs} - t_q$) binned in projected cluster centric radius, normalised by R_{200} , for satellite galaxies (triangles) split by stellar mass of the corresponding central galaxy (top), stellar mass (middle) and the number of galaxies within the group (bottom). The corresponding values for central galaxies (squares) and galaxies in the GZ-CENT-FIELD sample (circles) are shown and connected by the dashed lines to aid the reader.

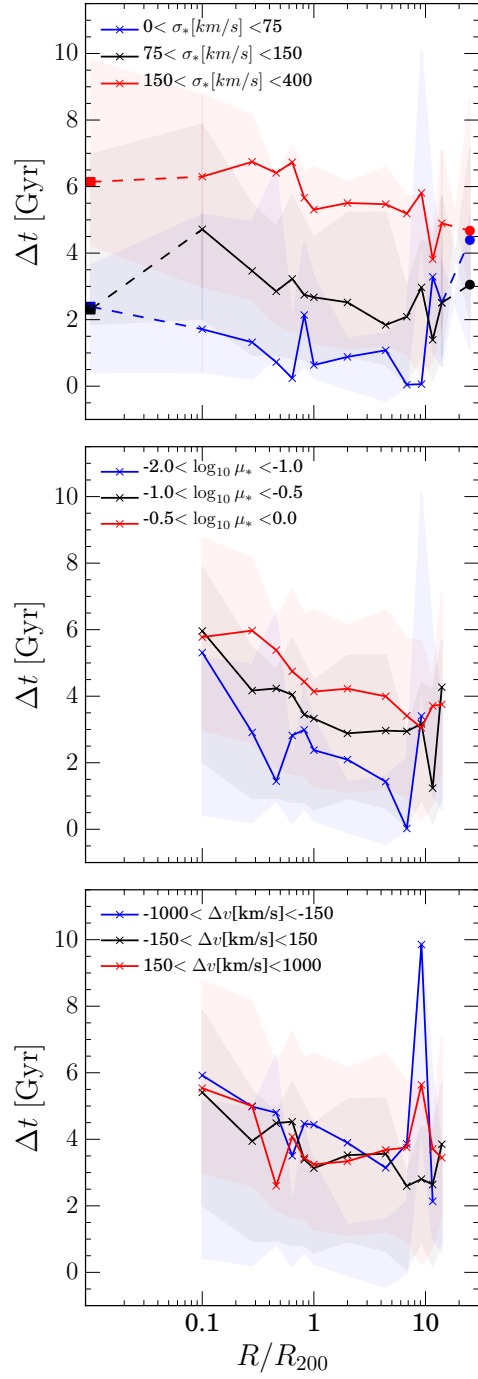


Figure 5.9: The time since quenching onset ($\Delta t = t_{\text{obs}} - t_q$) binned in projected cluster centric radius, normalised by R_{200} , for satellite galaxies (triangles) split by velocity dispersion (top), stellar mass ratio ($\mu_* = M_*/M_{*,c}$) (middle) and the difference in velocity from the associated central galaxy (bottom). The corresponding values for central galaxies (squares) and galaxies in the GZ-CENT-FIELD sample (circles) are shown and connected by the dashed lines to aid the reader in the top panel where appropriate.

due to the potential or temperature of the halo, but not dependant on the speed of the satellite. This suggests that ram pressure stripping is not the dominant environmental quenching mechanism at play.

We have shown that mergers are important for centrals not for satellites in the bottom panel of Figure 5.8. That mass quenching is important for satellites as well as centrals in the middle panel of Figure 5.8 and that larger halos have a stronger environmental effect on their satellites in the top panel of Figure 5.8.

Chapter 6

Discussion

In Section 4.1.2 we have discussed how our results of the changing morphological features and quenching timescales with projected cluster centric radius in the group environment show evidence for both merger driven, secular and environmentally driven evolutionary histories. This suggests that not one mechanism is dominant in the group environment but that a superposition of all these effects gives rise to the observed morphology-density and morphology-SFR relations.

All these mechanisms are striving towards the same end result with no single mechanisms dominating over the other. Those mechanisms traditionally associated with the field, such as secular evolution can also occur in more dense environments, however will often eventually be overwhelmed by those more rapid and violent mechanisms of mergers and interactions (and the triggered outflows from AGN that are associated with such mechanisms; see Smethurst et al. 2016). Similarly, the environmental quenching mechanisms are at work as soon as a galaxy falls into a group or cluster, but such a process can be interrupted momentarily by an interaction or a merger as a galaxy enters the more dense environment.

Just as morphology is a spectrum from disc-dominated to spheroid-dominated systems, so to are the quenching mechanisms which cause this morphological transformation. Mergers and interactions are a spectrum of mass ratios from the micro mergers (?) through to major mergers, with increasing impact upon the morphology and SFR of a galaxy. Secular quenching mechanisms are a spectrum of stellar mass, with a larger impact on those galaxies with smaller masses. Environmental quenching mechanisms are a spectrum of increasing halo potential, giving rise to a stronger

impact on the SFR of smaller mass galaxies in larger halos.

All of these mechanisms coalesce will give rise to the distributions in galaxy properties we see across the Universe through their constant interplay across cosmic time.

Chapter 7

Conlusions

Quenching is morphologically dependant.

AGN may be responsible for some of this quenching.

The environment plays less of a role than typical mass quenching.

Bibliography

- Abramson L. E., Gladders M. D., Dressler A., Oemler A., Poggianti B., Vulcani B., 2016, ArXiv e-prints, 1604.00016
- Arnouts S. et al., 2007, A&A, 476, 137
- Astropy Collaboration et al., 2013, A&A, 558, A33
- Baldry I. K., Balogh M. L., Bower R. G., Glazebrook K., Nichol R. C., Bamford S. P., Budavari T., 2006, MNRAS, 373, 469
- Baldry I. K., Glazebrook K., Brinkmann J., Ivezić Ž., Lupton R. H., Nichol R. C., Szalay A. S., 2004, ApJ, 600, 681
- Baldwin J. A., Phillips M. M., Terlevich R., 1981, PASP, 93, 5
- Ball N. M., Loveday J., Brunner R. J., 2008, MNRAS, 383, 907
- Bamford S. P. et al., 2009, MNRAS, 393, 1324
- Barro G. et al., 2013, ApJ, 765, 104
- Bell E. F., de Jong R. S., 2001, ApJ, 550, 212
- Bell E. F. et al., 2004, ApJ, 608, 752
- Berlind A. A. et al., 2006, ApJS, 167, 1
- Béthermin M. et al., 2012, ApJ, 757, L23
- Bower R. G., Benson A. J., Malbon R., Helly J. C., Frenk C. S., Baugh C. M., Cole S., Lacey C. G., 2006, MNRAS, 370, 645
- Bower R. G., Lucey J. R., Ellis R. S., 1992, MNRAS, 254, 601

- Brammer G. B. et al., 2009, ApJ, 706, L173
- Brinchmann J., Charlot S., White S. D. M., Tremonti C., Kauffmann G., Heckman T., Brinkmann J., 2004, MNRAS, 351, 1151
- Bruzual G., Charlot S., 2003, MNRAS, 344, 1000
- Buat V. et al., 2005, ApJ, 619, L51
- Canalizo G., Stockton A., 2001, ApJ, 555, 719
- Chabrier G., 2003, PASP, 115, 763
- Chen X. Y., Liang Y. C., Hammer F., Prugniel P., Zhong G. H., Rodrigues M., Zhao Y. H., Flores H., 2010, A&A, 515, A101
- Chester C., Roberts M. S., 1964, AJ, 69, 635
- Cheung E. et al., 2012, ApJ, 760, 131
- Coil A. L. et al., 2008, ApJ, 672, 153
- Conroy C., Gunn J. E., White M., 2009, ApJ, 699, 486
- Conselice C. J., Bershady M. A., Dickinson M., Papovich C., 2003, AJ, 126, 1183
- Constantin A., Hoyle F., Vogeley M. S., 2008, ApJ, 673, 715
- Cowie L. L., Barger A. J., 2008, ApJ, 686, 72
- Cowie L. L., Songaila A., Hu E. M., Cohen J. G., 1996, AJ, 112, 839
- Croton D. J. et al., 2006, MNRAS, 365, 11
- Daddi E. et al., 2007, ApJ, 670, 156
- Daddi E. et al., 2010, ApJ, 714, L118
- Darg D. W. et al., 2010, MNRAS, 401, 1043
- De Lucia G., Tornatore L., Frenk C. S., Helmi A., Navarro J. F., White S. D. M., 2014, MNRAS, 445, 970
- de Vaucouleurs G., 1953, MNRAS, 113, 134
- Di Matteo T., Springel V., Hernquist L., 2005, Nature, 433, 604

- Dressler A., 1980, ApJ, 236, 351
- Driver S. P. et al., 2006, MNRAS, 368, 414
- Elbaz D. et al., 2007, A&A, 468, 33
- Eminian C., Kauffmann G., Charlot S., Wild V., Bruzual G., Rettura A., Loveday J., 2008, MNRAS, 384, 930
- Emsellem E., Renaud F., Bournaud F., Elmegreen B., Combes F., Gabor J. M., 2015, MNRAS, 446, 2468
- Faber S. M. et al., 2007, ApJ, 665, 265
- Fabian A. C., 2012, ARA&A, 50, 455
- Falkenberg M. A., Kotulla R., Fritze U., 2009, MNRAS, 397, 1954
- Fang J. J., Faber S. M., Koo D. C., Dekel A., 2013, ApJ, 776, 63
- Foreman-Mackey D., Hogg D. W., Lang D., Goodman J., 2013, PASP, 125, 306
- Gabor J. M. et al., 2009, ApJ, 691, 705
- Glazebrook K. et al., 2003, ApJ, 587, 55
- Gómez P. L. et al., 2003, ApJ, 584, 210
- Gonçalves T. S., Martin D. C., Menéndez-Delmestre K., Wyder T. K., Koekemoer A., 2012, ApJ, 759, 67
- González V., Labb   I., Bouwens R. J., Illingworth G., Franx M., Kriek M., Brammer G. B., 2010, ApJ, 713, 115
- Goodman J., Weare J., 2010, CAMCS, 5, 65
- Graham A. W., 2001, AJ, 121, 820
- Greene J. E., Ho L. C., 2007, ApJ, 670, 92
- Haines T., McIntosh D. H., S  nchez S. F., Tremonti C., Rudnick G., 2015, MNRAS, 451, 433
- H  ring N., Rix H.-W., 2004, ApJ, 604, L89

- Hayward C. C., Torrey P., Springel V., Hernquist L., Vogelsberger M., 2014, MNRAS, 442, 1992
- Heinis S. et al., 2014, MNRAS, 437, 1268
- Hickox R. C. et al., 2009, ApJ, 696, 891
- Hopkins P. F., Cox T. J., Kereš D., Hernquist L., 2008, ApJS, 175, 390
- Ishibashi W., Fabian A. C., 2012, MNRAS, 427, 2998
- Jiang Y.-F., Greene J. E., Ho L. C., 2011, ApJ, 737, L45
- Kauffmann G. et al., 2003a, MNRAS, 346, 1055
- Kauffmann G. et al., 2003b, MNRAS, 341, 33
- Kaviraj S., 2014, MNRAS, 437, L41
- Kaviraj S. et al., 2013, MNRAS, 428, 925
- Kennicutt R. C., 1997, in Astrophysics and Space Science Library, Vol. 161, Astrophysics and Space Science Library, pp. 171–195
- Kennicutt, Jr. R. C., Roettiger K. A., Keel W. C., van der Hulst J. M., Hummel E., 1987, AJ, 93, 1011
- Kewley L. J., Groves B., Kauffmann G., Heckman T., 2006, MNRAS, 372, 961
- Kewley L. J., Heisler C. A., Dopita M. A., Lumsden S., 2001, ApJS, 132, 37
- Ko J., Hwang H. S., Lee J. C., Sohn Y.-J., 2013, ApJ, 767, 90
- Kormendy J., Kennicutt, Jr. R. C., 2004, ARA&A, 42, 603
- Koss M., Mushotzky R., Veilleux S., Winter L. M., Baumgartner W., Tueller J., Gehrels N., Valencic L., 2011, ApJ, 739, 57
- Kriek M. et al., 2010, ApJ, 722, L64
- Lahav O., Bridle S. L., Hobson M. P., Lasenby A. N., Sodré L., 2000, MNRAS, 315, L45
- Lintott C. et al., 2011, MNRAS, 410, 166

- Lintott C. J. et al., 2009, MNRAS, 399, 129
- Lintott C. J. et al., 2008, MNRAS, 389, 1179
- Mackay D. J. C., 2003, Information Theory, Inference and Learning Algorithms. p. 640
- Magorrian J. et al., 1998, AJ, 115, 2285
- Marasco A., Fraternali F., Binney J. J., 2012, MNRAS, 419, 1107
- Maraston C., 2005, MNRAS, 362, 799
- Marconi A., Hunt L. K., 2003, ApJ, 589, L21
- Martin D. C. et al., 2007, ApJS, 173, 342
- Masters K. L. et al., 2010a, MNRAS, 405, 783
- Masters K. L. et al., 2010b, MNRAS, 404, 792
- Masters K. L. et al., 2011, MNRAS, 411, 2026
- McIntosh D. H. et al., 2014, MNRAS, 442, 533
- McLure R. J., Dunlop J. S., 2001, MNRAS, 327, 199
- McLure R. J., Kukula M. J., Dunlop J. S., Baum S. A., O'Dea C. P., Hughes D. H., 1999, MNRAS, 308, 377
- Melbourne J. et al., 2012, ApJ, 748, 47
- Mendez A. J., Coil A. L., Lotz J., Salim S., Moustakas J., Simard L., 2011, ApJ, 736, 110
- Miner J., Rose J. A., Cecil G., 2011, ApJ, 727, L15
- Nair P. B., Abraham R. G., 2010, ApJL, 714, L260L264
- Nandra K. et al., 2007, ApJ, 660, L11
- Noeske K. G. et al., 2007, ApJ, 660, L43
- Oh K., Yi S. K., Schawinski K., Koss M., Trakhtenbrot B., Soto K., 2015, ApJS, 219, 1

- Pan Z., Li J., Lin W., Wang J., Kong X., 2014, ApJ, 792, L4
- Peng C. Y., Ho L. C., Impey C. D., Rix H.-W., 2002, AJ, 124, 266
- Peng C. Y., Ho L. C., Impey C. D., Rix H.-W., 2010, AJ, 139, 2097
- Peng Y.-j., Lilly S. J., Renzini A., Carollo M., 2012, ApJ, 757, 4
- Pierce C. M. et al., 2007, ApJ, 660, L19
- Pontzen A., Tremmel M., Roth N., Peiris H. V., Saintonge A., Volonteri M., Quinn T., Governato F., 2016, ArXiv e-prints, 1607.02507
- Sánchez S. F. et al., 2004, ApJ, 614, 586
- Salim S. et al., 2007, ApJS, 173, 267
- Sánchez-Blázquez P., Gorgas J., Cardiel N., González J. J., 2006, A&A, 457, 809
- Sanders D. B., Soifer B. T., Elias J. H., Madore B. F., Matthews K., Neugebauer G., Scoville N. Z., 1988, ApJ, 325, 74
- Sarzi M. et al., 2006, MNRAS, 366, 1151
- Sarzi M. et al., 2010, MNRAS, 402, 2187
- Schawinski K., Thomas D., Sarzi M., Maraston C., Kaviraj S., Joo S.-J., Yi S. K., Silk J., 2007, MNRAS, 382, 1415
- Schawinski K. et al., 2014, MNRAS, 440, 889
- Schawinski K. et al., 2010, ApJ, 711, 284
- Schawinski K., Virani S., Simmons B., Urry C. M., Treister E., Kaviraj S., Kushkuley B., 2009, ApJ, 692, L19
- Schiminovich D. et al., 2007, ApJS, 173, 315
- Schmidt M., 1959, ApJ, 129, 243
- Shen Y. et al., 2011, ApJS, 194, 45
- Silk J., Rees M. J., 1998, A&A, 331, L1
- Simard L., Mendel J. T., Patton D. R., Ellison S. L., McConnachie A. W., 2011, ApJS, 196, 11

- Simmons B. D. et al., 2013, MNRAS, 429, 2199
- Simmons B. D., Urry C. M., 2008, ApJ, 683, 644
- Simmons B. D., Van Duyne J., Urry C. M., Treister E., Koekemoer A. M., Grogin N. A., The GOODS Team, 2011, ApJ, 734, 121
- Singh R. et al., 2013, A&A, 558, A43
- Sivia D., Skilling J., 2006, Data Analysis: A Bayesian Tutorial, Oxford science publications. OUP Oxford
- Skibba R. A. et al., 2009, MNRAS, 399, 966
- Smethurst R. J. et al., 2016, MNRAS
- Smethurst R. J. et al., 2015, MNRAS, 450, 435
- Snyder G. F., Cox T. J., Hayward C. C., Hernquist L., Jonsson P., 2011, ApJ, 741, 77
- Somerville R. S., Hopkins P. F., Cox T. J., Robertson B. E., Hernquist L., 2008, MNRAS, 391, 481
- Springel V., Di Matteo T., Hernquist L., 2005, ApJ, 620, L79
- Strateva I. et al., 2001, AJ, 122, 1861
- Thomas D., Maraston C., Schawinski K., Sarzi M., Silk J., 2010, MNRAS, 404, 1775
- Tojeiro R., Heavens A. F., Jimenez R., Panter B., 2007, MNRAS, 381, 1252
- Tojeiro R. et al., 2013, MNRAS, 432, 359
- Tortora C., Antonuccio-Delogu V., Kaviraj S., Silk J., Romeo A. D., Becciani U., 2009, MNRAS, 396, 61
- Trager S. C., Faber S. M., Worthey G., González J. J., 2000, AJ, 120, 165
- Urry C. M., Scarpa R., O'Dowd M., Falomo R., Pesce J. E., Treves A., 2000, ApJ, 532, 816
- Varela J., Moles M., Márquez I., Galletta G., Masegosa J., Bettoni D., 2004, A&A, 420, 873

- Vazdekis A., Sánchez-Blázquez P., Falcón-Barroso J., Cenarro A. J., Beasley M. A., Cardiel N., Gorgas J., Peletier R. F., 2010, MNRAS, 404, 1639
- Wild V., Walcher C. J., Johansson P. H., Tresse L., Charlot S., Pollo A., Le Fèvre O., de Ravel L., 2009, MNRAS, 395, 144
- Willett K. W. et al., 2013, MNRAS, 435, 2835
- Willmer C. N. A. et al., 2006, ApJ, 647, 853
- Wright E. L. et al., 2010, AJ, 140, 1868
- Wyder T. K. et al., 2007, ApJS, 173, 293
- Yan R., Blanton M. R., 2012, ApJ, 747, 61
- Yesuf H. M., Faber S. M., Trump J. R., Koo D. C., Fang J. J., Liu F. S., Wild V., Hayward C. C., 2014, ApJ, 792, 84
- York D. G. et al., 2000, AJ, 120, 1579
- Zinn P.-C., Middelberg E., Norris R. P., Dettmar R.-J., 2013, ApJ, 774, 66